BLUR ESTIMATION AND SUPERRESOLUTION FROM MULTIPLE REGISTERED IMAGES

A THESIS SUBMITTED TO
THE GRADUATE SCHOOL OF NATURAL AND APPLIED SCIENCES
OF
MIDDLE EAST TECHNICAL UNIVERSITY

BY

ENGİN UTKU ŞENSES

IN PARTIAL FULFILLMENT OF THE REQUIREMENTS
FOR
THE DEGREE OF MASTER OF SCIENCE
IN
ELECTRICAL AND ELECTRONICS ENGINEERING

SEPTEMBER 2008

Approval of the thesis:

BLUR ESTIMATION AND SUPERRESOLUTION FROM MULTIPLE REGISTERED IMAGES

submitted by **ENGİN UTKU ŞENSES** in partial fulfillment of the requirements for the degree of **Master of Science in Electrical and Electronics Engineering Department, Middle East Technical University** by,

Prof. Dr. Canan Özgen _____
Dean, Graduate School of **Natural and Applied Sciences**

Prof. Dr. İsmet Erkmen _____
Head of Department, **Electrical and Electronics Engineering**

Assist. Prof. Dr. İlkay Ulusoy _____
Supervisor, **Electrical and Electronics Engineering Dept., METU**

Examining Committee Members:

Prof. Dr. Gözde Bozdağı Akar _____
Electrical and Electronics Engineering Dept., METU

Assist. Prof. Dr. İlkay Ulusoy _____
Electrical and Electronics Engineering Dept., METU

Assist. Prof. Dr. Çağatay Candan _____
Electrical and Electronics Engineering Dept., METU

Prof. Dr. Yasemin Yardımcı Çetin _____
Informatics Institute, METU

Assist. Prof. Dr. Hasan Şakir Bilge _____
Computer Engineering Dept., Gazi University

Date: September 03, 2008

I hereby declare that all information in this document has been obtained and presented in accordance with academic rules and ethical conduct. I also declare that, as required by these rules and conduct, I have fully cited and referenced all material and results that are not original to this work.

Name, Last name : Engin Utku Şenses

Signature :

ABSTRACT

BLUR ESTIMATION AND SUPERRESOLUTION
FROM
MULTIPLE REGISTERED IMAGES

Şenses, Engin Utku
M.S., Department of Electrical and Electronics Engineering
Supervisor: Assist. Prof. Dr. İlkay Ulusoy

September 2008, 84 pages

Resolution is the most important criterion for the clarity of details on an image. Therefore, high resolution images are required in numerous areas. However, obtaining high resolution images has an evident technological cost and the value of these costs change with the quality of used optical systems. Image processing methods are used to obtain high resolution images with low costs. This kind of image improvement is named as superresolution image reconstruction.

This thesis focuses on two main titles, one of which is the identification methods of blur parameters, one of the degradation operators, and the stochastic SR image reconstruction methods. The performances of different stochastic SR image reconstruction methods and blur identification methods are shown and compared. Then the identified blur parameters are used in superresolution algorithms and the results are shown.

Keywords: Superresolution, Blur Estimation / Identification, Image Reconstruction, Image Enhancement.

ÖZ

HİZALANMIŞ ÇOKLU RESİMLERDEN BULANIKLIK TAHMİNİ
VE
SÜPER ÇÖZÜNÜRLÜKLÜ GÖRÜNTÜ ELDE ETME

Şenses, Engin Utku

Yüksek Lisans, Elektrik – Elektronik Mühendisliği Bölümü

Tez Yöneticisi: Yrd. Doç. Dr. İlkay Ulusoy

Eylül 2008, 84 sayfa

Çözünürlük bir görüntü üzerindeki detayların belirginliği açısından önem teşkil eden ölçütlerin en başında gelmektedir. Bu yüzdendir ki günümüzde yüksek çözünürlüklü görüntüler artık birçok alanda aranır olmuştur. Ancak yüksek çözünürlüklü görüntü elde etmenin teknolojik olarak belirgin bir maliyeti mevcuttur ve bu miktarlar kullanılan optik sistemlerin kalitesine göre değişmektedir. Daha az maliyetle yüksek çözünürlüklü görüntü elde etmek için görüntü işleme yöntemleri kullanılmaktadır. Bu şekilde yüksek çözünürlüklü görüntü elde etme işlemi süper çözünürlüklü görüntü oluşturma olarak adlandırılır.

Bu tez, görüntü çözünürlüğünü bozan etkenlerden biri olan bulanıklığın tahmin edilmesi yöntemleri ve istatistiksel süper çözünürlük metotları olmak üzere iki temel başlık üzerinde yoğunlaşmıştır. Farklı istatistiksel süper çözünürlük modellerinin ve bulanıklık tahmini yöntemlerinin başarıları gösterilmiş ve karşılaştırılmıştır. Daha sonra tahmin edilen bulanıklık değerleri, süper çözünürlük algoritması içerisinde kullanılmış ve sonuçlar gösterilmiştir.

Anahtar Kelimeler: Süper Çözünürlük, Bulanıklık Tahmini / Tanımlama, İmge Yapılandırılması, İmge İyileştirme.

To My Family

ACKNOWLEDGEMENTS

First of all, I would like to thank my supervisor Assist. Prof. Dr. İlkay Ulusoy for her guidance, encouragement, support and patience throughout the preparation of this thesis. I am grateful to my colleague Özgür Çevik, my friends Orkun Sunar and Sabri Can Bozdemir for their encouraging me in the development, for their valuable suggestions and support during this thesis. Special thanks to Berkan Solmaz and Umut Demirezen for their interest.

Thanks to my institute TÜBİTAK – UEKAE for the support of scientific research. And my grateful thanks to my family for their moral support all the time.

TABLE OF CONTENTS

LIST OF TABLES

TABLES

LIST OF FIGURES

FIGURES

LIST OF ABREVIATIONS

SR	Superresolution
HR	High Resolution
LR	Low Resolution
IBP	Iterated Back Projection
CCD	Charged Coupled Device
CMOS	Complementary Metal Oxide Semiconductor
CFT	Continuous Fourier Transform
DFT	Discrete Fourier Transform
POCS	Projection onto Convex Sets
PDF	Probability Density Function
ML	Maximum Likelihood
WLS	Weighted Least Squares
MAP	Maximum a Posteriori Estimation
PSF	Point Spread Function
ARMA	Auto Regressive Moving Average
AR	Auto Regressive
MA	Moving Average
MRF	Markov Random Fields
TV	Total Variation
BTV	Bilateral Total Variation
MSE	Mean Square Error
PSNR	Peak Signal Noise Ratio
σ	Variance
φ	Angle

CHAPTER 1

INTRODUCTION

The number of the elements (pixels) that represent a digital image is known as the resolution. It can be said that the resolution of the image is directly proportional to the number of the pixels in the image. High resolution (HR) is a required characteristic in many areas. For instance, medical images, the images must be HR for correct diagnosis. Also HR images can be used to evaluate any situation correctly on the place that is watched by camera for surveillance applications. On the other hand, the requirements to HR images are increasing due to technological improvement day by day.

In the last two decades big revolutions become real in the digital imaging. Upgraded cameras have the ability to save HR images. In these cameras Charged Coupled Device (CCD) and Complementary Metal Oxide Semiconductor (CMOS) sensors are used. Photodiodes are placed inside these sensors and by increasing the number of these photodiodes the pixel level increases. The pixel level is proportional to the photodiodes. High pixel level promotes image resolution. General purposed cameras have 30000 – 50000 photodiodes which have sizes change between 2µm - 10µm. HR images can be acquired by decreasing the photo sensitive diode size, consequently the pixel size. Nowadays sensors are developed that use diodes smaller than 0.35 µm. By this development 39 mega pixel images are reached in the professional photography. But because of the high prices, these cameras can be used only in limited areas.

The physical and the economical limitations direct the people to find new solutions for obtaining HR images that are cheaper and easier. In this situation signal

processing techniques meet peoples need. The applications of signal processing techniques enable to generate HR images by using low resolution images. This process is named as “generation of superresolution image”.

The main idea of superresolution (SR) is to create HR images by using different low resolution (LR) images which include to the same scene. But it could not be said that HR images can be created by only increasing the pixel number. Although pixel expresses the resolution, the aim of generating HR image is to uncover the details of the scene besides increasing the number of pixels. These details carry high frequency information of the image. This process can be done by two ways: 1-) SR Restoration is the process that produces HR image without changing the image size, 2-) SR Reconstruction uses LR images for increasing pixel level and increasing image details of the scene.

Digital image is exposed to some effects during recording. These effects can be listed as blurring, motion, decimation and noise. To reach a HR image from LR ones, the exposed effects have to be removed.

There are two main approaches which are used to generate HR images. These are frequency domain approaches and pixel domain approaches. Various methods have been proposed under each approach and these are classified as follows:

- ✓ Frequency Domain Approaches:
  - Least Squares Approximation Methods,
  - Recursive Least Squares Approximation Methods,
  - Multichannel Sampling Theorem Methods,
- ✓ Spatial Domain Approaches:
  - Iterated Back Projection (IBP) Methods,
  - Deterministic Methods,
  - Set Theoretic Methods,
  - Stochastic Methods,
  - Hybrid Methods.

The scope of this thesis is to find the blurring parameters, one of the effects that decrease the resolution, and to create HR images by using one of the well known methods of spatial domain approaches, stochastic methods, where the estimated blurring parameter is considered also.

This thesis consists of six chapters. In Chapter 1, a brief introduction of digital imaging and SR methodology is given. In Chapter 2, observation model of LR images is explained. The matrix and the mathematical forms are also derived. In Chapter 3, SR approaches are surveyed. In Chapter 4, blur estimation / identification methods are surveyed. In Chapter 5, experimental studies for Stochastic Methods and blur parameter estimation / identification methods are shown. SR methods are applied with the known and the estimated / identified blur parameters. Chapter 6 provides the conclusions for the overall study. Throughout the thesis, the implementations of the methods are generated using MATLAB. The methods are examined and analyses of the methods are performed under various blur conditions with different sized images.

CHAPTER 2

LOW RESOLUTION IMAGE FORMATION MODEL

SR is an ill posed inverse problem because of the effects that degrade the image frame during the record of the scene. Some of these effects are caused by the limitations of the used camera, as insufficient number of CCD sensors and the continuous Point Spread Functions (PSF). The motion between the scene and the camera during the record causes warping [22]. And the insufficient amount of light of the environment can cause noise. Also the atmospheric conditions cause extra blur to the scene. The schematically description of these effects is given in Figure 2.1.

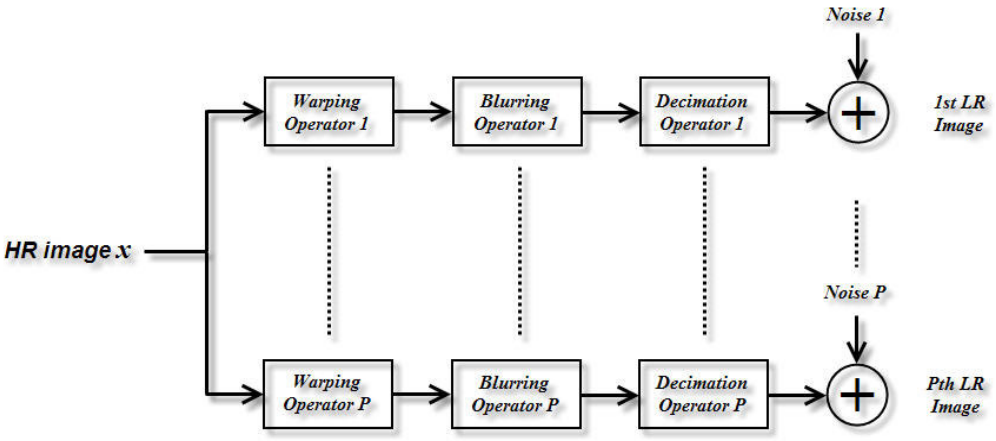

Figure 2.1 Schematic of the LR observation model.

In this chapter, model of the LR image formation is explained. The matrix forms of the degradation operators will be shown with examples and the mathematical forms of the degradation operators will be derived. The explanation of how to create

registered LR images for the tests is given and also an example of registered LR image formation is given.

2.1. Observation Model of Low Resolution Images

The general observation model of the LR image with all of the degradation effects can be given as,

$$\underline{y}_i = D H_i F_i \underline{x} + \underline{n}_i, \qquad i = 1, 2, ..., p \tag{2.1}$$

where

- ✓ '$\underline{y}$' is the lexicographically ordered vector form of LR image of size $1 \times n_1 n_2$,
- ✓ 'D' is the matrix form of the decimation operator of size $n_1 n_2 \times q_1 q_2 n_1 n_2$, ($q_1$ and q_2 are the decimation ratios in vertical and horizontal directions),
- ✓ 'H' is the matrix form of blurring operator of size $q_1 q_2 n_1 n_2 \times q_1 q_2 n_1 n_2$,
- ✓ 'F' is the matrix form of warping operator of size $q_1 q_2 n_1 n_2 \times q_1 q_2 n_1 n_2$,
- ✓ '$\underline{x}$' is the lexicographically ordered vector form of original HR image of size $1 \times q_1 q_2 n_1 n_2$,
- ✓ '$\underline{n}$' is the vector form of noise of size $1 \times q_1 q_2 n_1 n_2$,
- ✓ 'p' is the number of available LR image frames.

The decimation matrix symbolizes the sampling operation. In the classic sampling theory, the samples take the value of the continuous function at that time as seen in Figure 2.2 as one dimension [28].

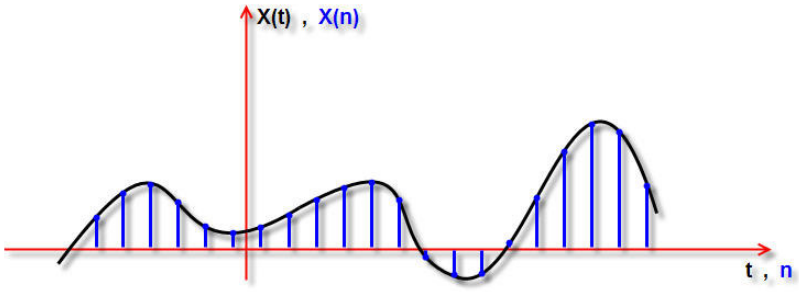

Figure 2.2 Example of Classic Sampling.

In the cameras, the focused light luminous energy on the CCD sensor creates electrical energy on the cells. The output of the cell is the sum of these energies [28]. This can be shown in Figure 2.3 in one dimension. This is also an integration of the luminance values.

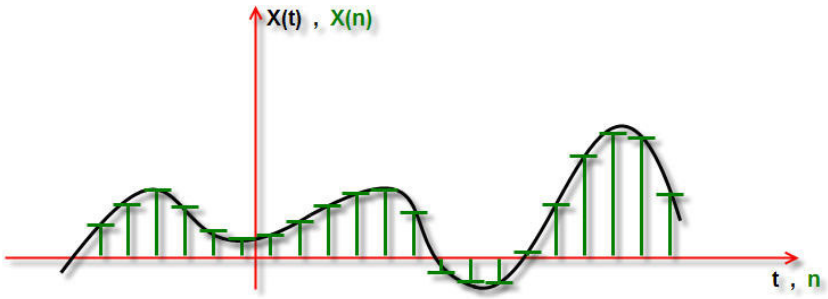

Figure 2.3 Example of Area Sampling.

This effect can be seen in the figure below where the pixel intensity value takes the average of the luminance values. Hence the spaces between the pixels shown in Figure 2.4 are very small; these values are neglected in the calculations.

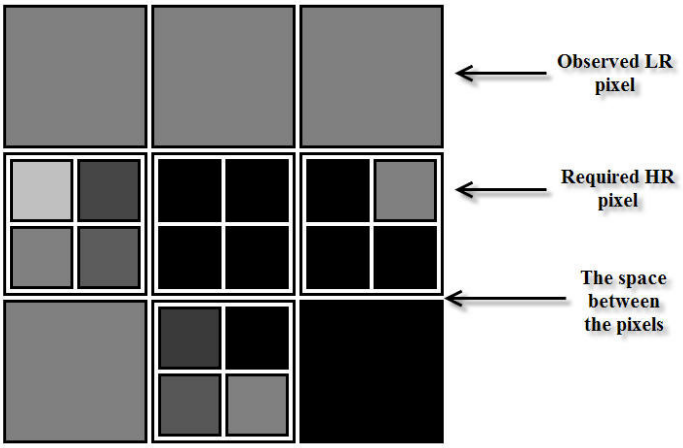

Figure 2.4 The HR pixels and LR pixel formation model.

In our implementations the warping effect is assumed to be known. So the warping operator is not used in our image model. The warping operations and registration operations are done out of the model. Hence, the image formation model of our implementations is reduced to the form shown in (2.2). The used algorithm for creating registered LR test image formation is given in part 2.4.

$$\underline{y}_i = D H_i \underline{x} + \underline{n}_i , \qquad i = 1, 2, ..., p . \tag{2.2}$$

2.2. Matrix Forms of Degradation Parameters

As mentioned before the matrix form of D is sized as $n_1 n_2 \times q_1 q_2 n_1 n_2$ and it has a form shown as below [23 - 25].

$$D = \frac{1}{q_1 q_2} \begin{bmatrix} 1 & \cdots & 1 & & \cdots & & \cdots & & \cdots & & 0 \\ & & \vdots & & & & & & & & \\ \vdots & & & 1 & \cdots & 1 & & & \ddots & & \vdots \\ & & & & \ddots & \vdots & & \ddots & & & \\ \vdots & & & \ddots & & & 1 & \cdots & 1 & & \vdots \\ & & & & & & & & \vdots & & \\ 0 & & \cdots & & \cdots & & \cdots & & 1 & \cdots & 1 \end{bmatrix} \tag{2.3}$$

An example D decimation matrix for a 4×4 sized image with $q_1 = q_2 = 2$ that decreases the image dimensions to 2×2 can be given as,

$$D = \frac{1}{2^2}\begin{bmatrix} 1 & 1 & 0 & 0 & 1 & 1 & 0 & 0 & 0 & 0 & 0 & 0 & 0 & 0 & 0 & 0 \\ 0 & 0 & 1 & 1 & 0 & 0 & 1 & 1 & 0 & 0 & 0 & 0 & 0 & 0 & 0 & 0 \\ 0 & 0 & 0 & 0 & 0 & 0 & 0 & 0 & 1 & 1 & 0 & 0 & 1 & 1 & 0 & 0 \\ 0 & 0 & 0 & 0 & 0 & 0 & 0 & 0 & 0 & 0 & 1 & 1 & 0 & 0 & 1 & 1 \end{bmatrix} \tag{2.4}$$

The H is the matrix of blurring kernel. The dimensions of the blurring kernel are smaller than the image dimensions, for example 5×5 or 7×7. It depends on the PSF effect of the used camera. The blurring kernel and its matrix form are shown below.

$$h = \begin{bmatrix} \ddots & & \vdots & & \iddots \\ & h_{i-1,j-1} & h_{i-1,j} & h_{i-1,j+1} & \\ \cdots & h_{i,j-1} & h_{i,j} & h_{i,j+1} & \cdots \\ & h_{i+1,j-1} & h_{i+1,j} & h_{i+1,j+1} & \\ \iddots & & \vdots & & \ddots \end{bmatrix} \tag{2.5}$$

$$H = \begin{bmatrix} h_{i,j} & h_{i,j+1} & \cdots & \cdots & h_{i+1,j} & h_{i+1,j+1} & \cdots & & \cdots \\ h_{i,j-1} & h_{i,j} & h_{i,j+1} & & h_{i,j-1} & h_{i+1,j} & h_{i+1,j+1} & & \\ \cdots & h_{i,j-1} & h_{i,j} & h_{i,j+1} & \cdots & h_{i,j-1} & h_{i,+1j} & h_{i+1,j+1} & \\ \vdots & & & \ddots & & & & \ddots & \\ h_{i-1,j} & h_{i,j+1} & & & \ddots & & & & \\ h_{i-1,j+1} & h_{i-1,j} & h_{i,j+1} & & & \ddots & & & \\ \vdots & h_{i-1,j-1} & h_{i-1,j} & h_{i,j+1} & & h_{i,j-1} & h_{i,j} & h_{i,j+1} & \\ & & & \ddots & & & h_{i,j-1} & h_{i,j} & h_{i,j+1} \\ \vdots & & & & & & \cdots & h_{i,j-1} & h_{i,j} \end{bmatrix} \tag{2.6}$$

An example 3×3 dimension h blurring kernel (2.7) and corresponding 16×16 H blurring matrix (2.8) for a 4×4 sized image are shown below.

$$h = \frac{1}{15}\begin{bmatrix} 1 & 2 & 1 \\ 2 & 3 & 2 \\ 1 & 2 & 1 \end{bmatrix} \tag{2.7}$$

$$H = \frac{1}{15}\begin{bmatrix}
3 & 2 & 0 & 0 & 2 & 1 & 0 & \cdots & \cdots & & 0 & & & & 0 \\
2 & 3 & 2 & 0 & 1 & 2 & 1 & \ddots & & \ddots & & & & \iddots & \\
0 & 2 & 3 & 2 & 0 & 1 & 2 & 1 & & & & & 0 & & \\
0 & 0 & 2 & 3 & 2 & 0 & 1 & 2 & 1 & & & \iddots & & & \\
2 & 1 & 0 & 2 & 3 & 2 & 0 & 1 & 2 & 1 & 0 & & & & \\
1 & 2 & 1 & 0 & 2 & 3 & 2 & 0 & 1 & 2 & 1 & & & & 0 \\
0 & 1 & 2 & 1 & 0 & 2 & 3 & 2 & 0 & 1 & 2 & 1 & & \ddots & \\
\vdots & \ddots & 1 & 2 & 1 & 0 & 2 & 3 & 2 & 0 & 1 & 2 & 1 & & \vdots \\
\vdots & & & 1 & 2 & 1 & 0 & 2 & 3 & 2 & 0 & 1 & 2 & \ddots & \vdots \\
 & \ddots & & & 1 & 2 & 1 & 0 & 2 & 3 & 2 & 0 & 1 & 2 & 1 & 0 \\
0 & & & & & 1 & 2 & 1 & 0 & 2 & 3 & 2 & 0 & 1 & 2 & 1 \\
 & & & & 0 & & 1 & 2 & 1 & 0 & 2 & 3 & 2 & 0 & 1 & 2 \\
\vdots & & & \iddots & & & & 1 & 2 & 1 & 0 & 2 & 3 & 2 & 0 & 1 \\
\vdots & & 0 & & & & & & 1 & 2 & 1 & 0 & 2 & 3 & 2 & 0 \\
 & \iddots & & & & & \ddots & & \ddots & 1 & 2 & 1 & 0 & 2 & 3 & 2 \\
0 & & \cdots & \cdots & & 0 & & \cdots & \cdots & 0 & 1 & 2 & 1 & 0 & 2 & 3
\end{bmatrix} \tag{2.8}$$

The noise is in vector form of the same size of lexicographically ordered LR image frame.

2.3. Mathematical Forms of Degradation Parameters

If we remember our observation model mentioned above,

$$\underline{y}_i = D H_i \underline{x} + \underline{n}_i, \qquad i = 1, 2, ..., p, \tag{2.9}$$

we can see that the HR image $\underline{x}$ is first blurred with a smoothing kernel. This smoothing operation can be done by two dimensional convolution in spatial domain:

$$a_{i,j} = h(i,j) * x(i,j), \tag{2.10}$$

$$a(i,j) = \sum_{k=0}^{N_1-1} \sum_{l=0}^{N_2-1} h(k,l)x(i-k, j-l). \tag{2.11}$$

Then the size of the smoothed image obtained by convolution is reduced by down sampling procedure [23 - 25]:

$$b(i,j) = \frac{1}{q_1 q_2} \sum_{k=q_1 i}^{(q_1+1)i-1} \sum_{l=q_2 j}^{(q_2+1)i-1} a(k,l). \tag{2.12}$$

In the last step, the noise is added to the blurred, decimated image.

$$y(i,j) = b(i,j) + n(i,j). \tag{2.13}$$

In our implementations the noise is assumed to be zero mean, independent and identically distributed (i.i.d.). Then the probability density function (PDF) of the noise can be given as [24, 25]:

$$P(n_i) = \frac{1}{(2\pi)^{\frac{MN}{2}} \sigma_\eta^{MN}} \exp\left(-\frac{1}{2\sigma_\eta^2} n_i^T n_i \right). \tag{2.14}$$

Here σ_η^2 denotes the variance of the noise. The reconstruction problem now reduces to estimating x given y_i's, which is clearly an ill-posed, inverse problem.

2.4. Creation of Registered Low Resolution Images

As mentioned before the warping parameters are assumed to be known in this thesis study and the registration operations are done out of the LR image formation model.

Warping may contain global or local translation, rotation, shifts, etc. But for simplicity only the horizontal and vertical shifts are considered. The applied steps of registered LR frame creation shown schematically in Figures 2.6 and 2.7 are:

- ✓ original HR frame boundaries are filled with zeros,
- ✓ zero filled image is resampled by a factor of 2 in each dimensions,
- ✓ new image is shifted with double of the given subpixel values in x and y dimensions,
- ✓ shifted image is down sampled by a factor of 2 in each dimensions,
- ✓ the zero boundaries of the image are eliminated,
- ✓ image is convolved with a blurring kernel,
- ✓ blurred image is downsampled by a factor of 2,
- ✓ a Gaussian noise of a variance 5 is added,
- ✓ blurred noise added LR frame boundaries are filled with zeros,
- ✓ zero filled image is resampled by a factor of 2 in each dimensions,
- ✓ new image is shifted with double of the given subpixel values (half negative values of the first subpixel shift values) in x and y dimensions,
- ✓ shifted image is down sampled by a factor of 2 in each dimensions,
- ✓ the zero boundaries of the registered LR image frame are eliminated.

The new pixel values (Figure 2.5) are calculated as follows (2.15 – 2.19):

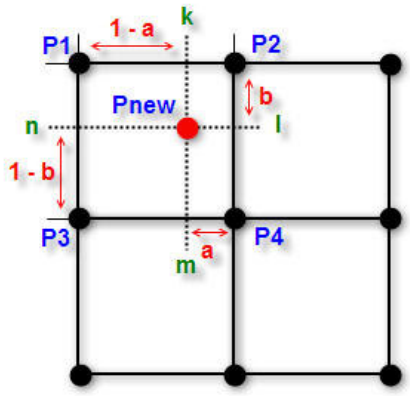

Figure 2.5 Shifted pixel value calculation

$$k = a \times P1 + (1 - a) \times P2\,, \tag{2.15}$$

$$l = P2 \times (1 - b) + P4 \times b\,, \tag{2.16}$$

$$m = P3 \times a + P4\,(1 - a)\,, \tag{2.17}$$

$$n = P1 \times (1 - b) + P3 \times b\,, \tag{2.18}$$

$$Pnew = \big(k \times (1 - b) + m \times b + l \times (1 - a) + n \times a\big) / 2\ . \tag{2.19}$$

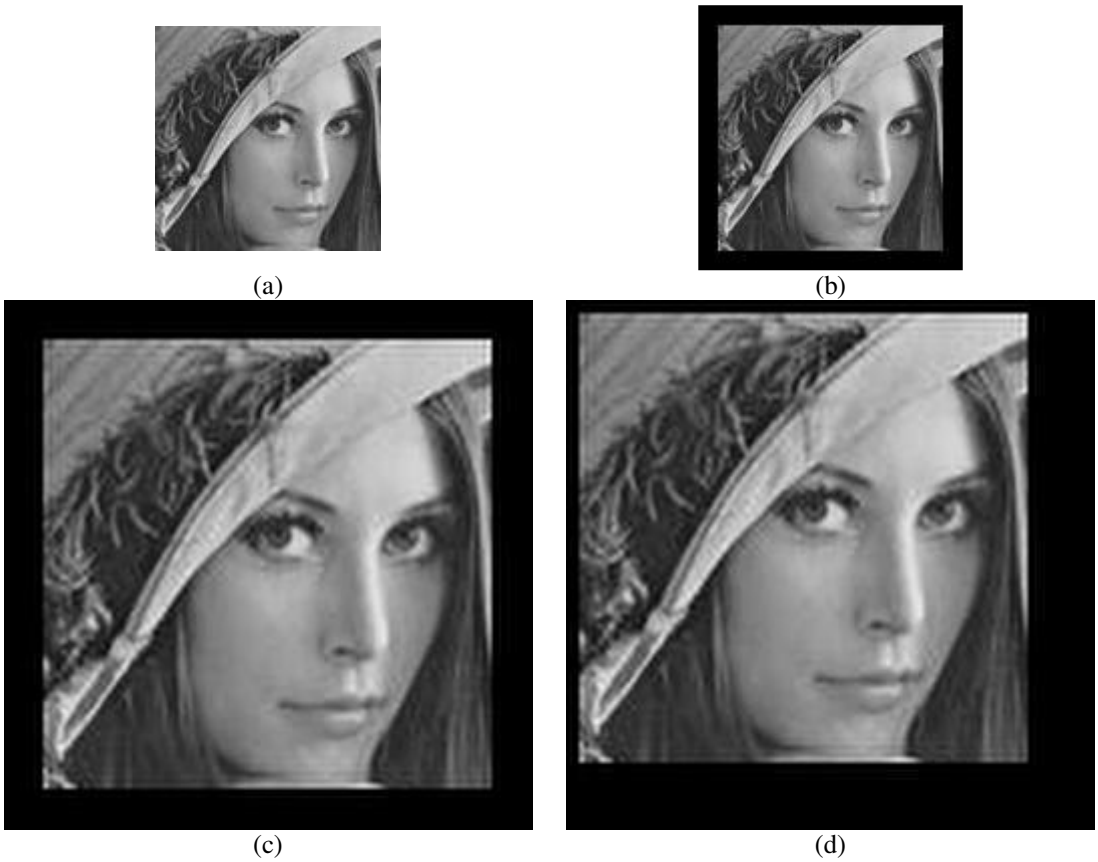

(a) (b) (c) (d)

Figure 2.6 The original HR frame (a) boundaries are filled with zeros (b). (c) shows the resampled image and (d) shows the subpixel shifted image.

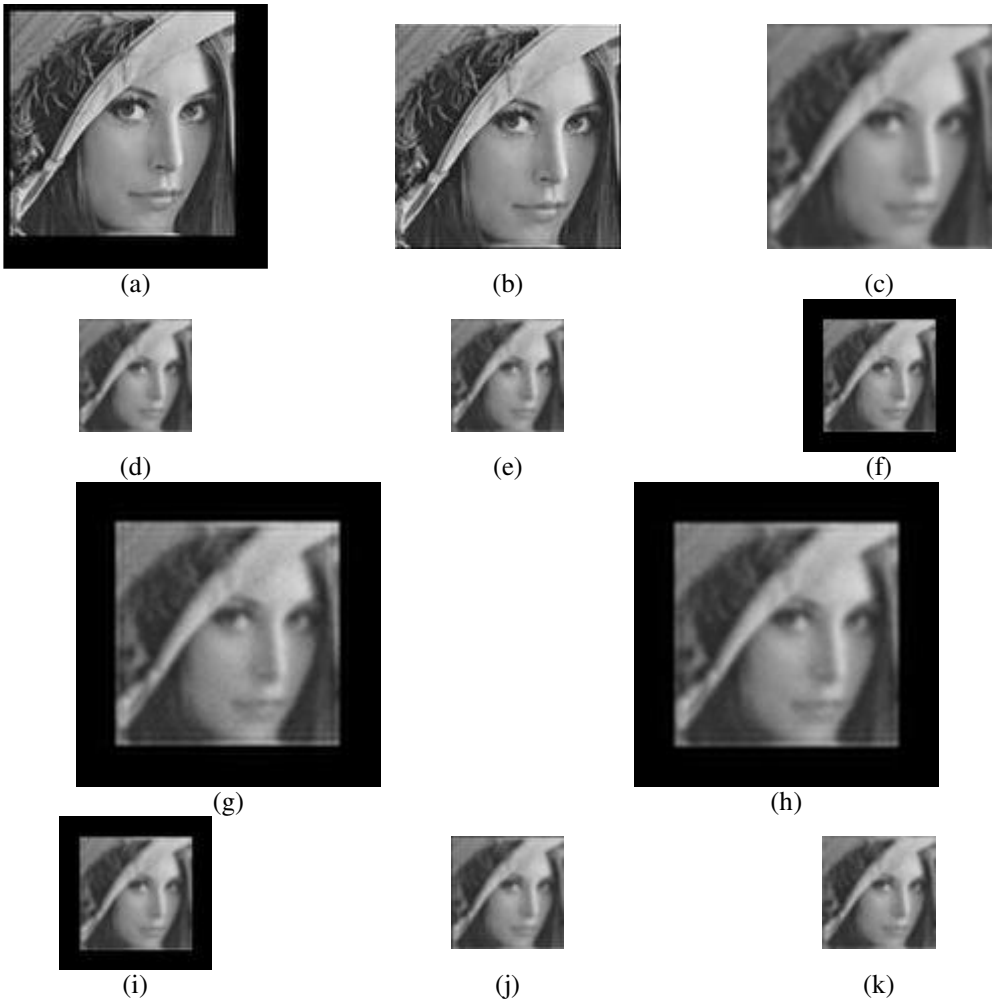

Figure 2.7 Boundary zeros of down sampled image (a) are eliminated (b). Image is blurred by a blurring kernel (c), down sampled (d) and added noise (e). The LR frame boundaries are filled with zeros (f). Image is resampled (g) and shifted with subpixel values (h). The boundaries of down sampled image (i) are eliminated (j). (k) shows the reference LR image frame.

CHAPTER 3

SUPERRESOLUTION METHODS

SR image reconstruction aims to create a HR image from a sequence of LR images of a scene. The main expectation of the application is to reach an upper sized and more detailed image.

While recording the scene information by a digital camera some effects based on atmosphere and hardware cause some information lost about the scene. These effects could be classified as follows:

- ✓ blur effect caused by the atmospheric conditions,
- ✓ blur effect caused by the PSF of the sensors,
- ✓ motion effect,
- ✓ insufficient photodiode number of the sensors,
- ✓ noise caused by the sensors.

The main idea of SR image reconstruction is to combine the LR data to upper size grid as shown in Figure 3.1.

SR is first mentioned by R.Y. Tsai and T.S. Huang in 1984 [1]. They used frequency domain approach on a set of decimated and shifted versions of an aerial image scene. They did not use blur and noise in their image model.

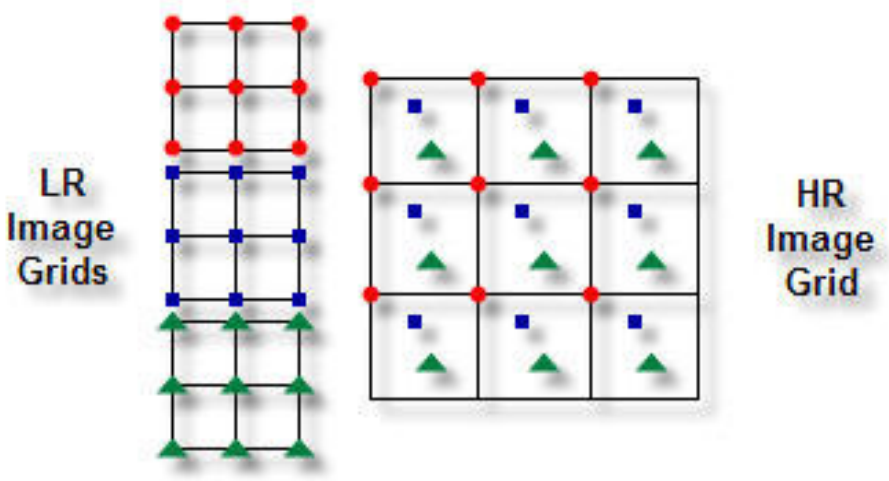

Figure 3.1 Observed and required resolution grids.

As mentioned before, there exists two SR approaches in the literature: frequency domain and spatial domain approaches. The frequency domain approach methods are based on three main principles [27]:

i. the shifting property of the Fourier Transform,
ii. the aliasing relationship between the Continuous Fourier Transform (CFT) of a HR image and Discrete Fourier Transform (DFT) of observed LR f images,
iii. the assumption that an original HR image is band limited.

These properties make it possible to formulate the system equation relating the aliased DFT coefficients of the observed LR images to a sample of the CFT of an unknown image.

Kim et.al. handled the frequency domain approach technique presented by Tsai and Huang and added blur and noise to their image model and developed an algorithm based on weighted recursive least squares theory [2]. M.Tekalp et.al. continued the method used in [1, 2] and denoted the blur as the point PSF of the sensors [3]. They solved the problem by using least squares approximation. A two step procedure

including up sampling and restoration of blur is given. And they showed the Projection onto Convex Sets (POCS) formulation as a method for the restoration of spatially variant blurred images and also multichannel sampling theorem methods are also discussed in [4, 5].

Frequency domain approaches are simple to implement, because the relationship of the LR images and the HR image can be shown easily in frequency domain. The methods have low computational complexity that reduces the hardware requirement. One of the disadvantages of the frequency domain approach is the limitation of the observation model. The model only includes global translation and linear space invariant degradation. And it is hard to implement the spatial domain *a-priori* knowledge for regularization [6].

Spatial domain approach is the second solution procedure of SR. In this procedure extraction of model formulation and the SR calculations are done in spatial domain. The linear spatial domain model can accommodate global and non-global motion, optical blur, motion blur, spatially varying PSF, non-ideal sampling, compression artifacts and more [6]. Spatial domain methods make it possible to include spatial domain *a-priori* knowledge to reconstruction.

The major spatial domain methods can be listed as follows:

- ✓ Iterated Back Projection (IBP) Methods
- ✓ Deterministic Methods
- ✓ Set Theoretic Methods
- ✓ Stochastic Methods
- ✓ Hybrid Methods

IBP methods depend on simulate and improve methodology. By using the initial estimate of SR image and the degradation model, new simulated images are created. Then the error between the observed images and the new simulated images is

calculated. Then this error value is back projected to update the initial estimate of HR image. This procedure is continued until the error is minimized to a desired value (Figure 3.2).

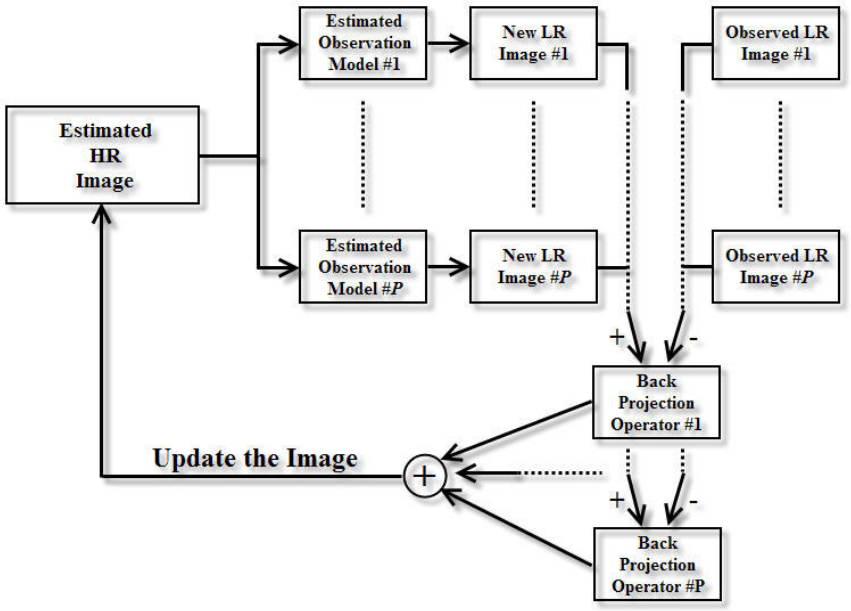

Figure 3.2 Schematical description of IBP.

The mathematical description of IBP cost function (3.1) in minimum least square sense and iterative formula (3.2), differentiated cost function with respect to $\underline{x}$, can be given as:

$$\left[\sum_{k=1}^{p}\left\|\underline{y}_k - W_k\,\underline{x}\right\|^2\right] \tag{3.1}$$

$$\begin{aligned}\hat{\underline{x}}^{(n+1)} &= \hat{\underline{x}}^{(n)} + \alpha\left(\sum_{k=1}^{p} W_k^{BP}\left(\underline{y}_k - \hat{\underline{y}}_k^{(n)}\right)\right)\\ &= \hat{\underline{x}}^{(n)} + \alpha\left(\sum_{k=1}^{p} W_k^{BP}\left(\underline{y}_k - W_k\,\hat{\underline{x}}^{(n)}\right)\right)\end{aligned} \tag{3.2}$$

where W is the observation model and W^{BP} is the back projection operator. Example of IBP methods can be found in [7, 8].

Deterministic SR approaches solve the ill posed inverse problem by using the prior information. The only difference of deterministic methods from IBP methods is the added regularization term that represents the prior information. The aim of deterministic methods is to minimize the cost function in regularized least squares sense:

$$\left[\sum_{k=1}^{p}\left\|\underline{y}_k - W_k\,\underline{x}\right\|^2 + \beta\left\|C\,\underline{x}\right\|^2\right]. \tag{3.3}$$

Differentiating the cost function with respect to $\underline{x}$ and setting to zero gives the iterative formula:

$$\begin{aligned}\underline{\hat{x}}^{(n+1)} &= \underline{\hat{x}}^{(n)} + \alpha\left(\sum_{k=1}^{p} W_k^T\,(\underline{y_k} - \underline{\hat{y}}_k^{(n)}) - \beta C^T C\,\underline{\hat{x}}^{(n)}\right)\\ &= \underline{\hat{x}}^{(n)} + \alpha\left(\sum_{k=1}^{p} W_k^T\,(\underline{y}_k - W_k\,\underline{\hat{x}}^{(n)}) - \beta C^T C\,\underline{\hat{x}}^{(n)}\right)\end{aligned} \tag{3.4}$$

where W is the observation model, α is the regularization parameter and C generally represents a high pass filter.

POCS is the generally used method in set theoretic reconstruction. The method is popular because of its simplicity [6]. Set theoretic methods use some constraint sets such as smoothness, bounded energy, fidelity to data, positivity, etc. The aim of the POCS method is to find a common point in the intersection of these (convex) constraint sets in the SR solution space shown in Figure 3.3. POCS is an iterative procedure and if the process convergences it will be in the first few iterations [9].

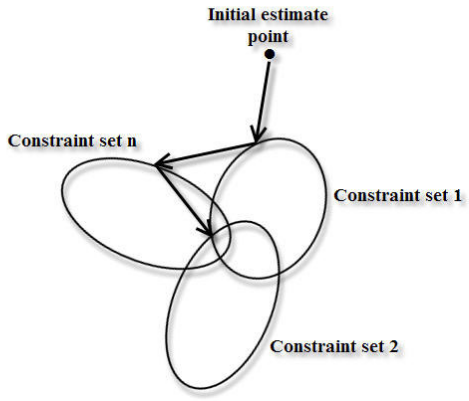

Figure 3.3 Schematic of the POCS Algorithm.

While the observation model is given as,

$$y_p = W_p x \tag{3.5}$$

where W represents the degradation model, constraint sets are formulated as in (3.6).

$$C_i = \{x : |y - W x| < \delta_0\} \tag{3.6}$$

where C_i denotes the constraint set. The solution point $\hat{x}$ lies in the intersection of all constraint sets.

$$\hat{x} \in C = \bigcap_{k=1}^{l} C_k \tag{3.7}$$

The initial points $\hat{x}_{i,j}$ must be chosen consistent to all constraint sets. The solution point can be found by applying projection operator to the corresponding constraint set as follows:

$$\underline{\hat{x}}^{(n+1)} = P_1 P_2 P_3 .... P_p \, \underline{\hat{x}}^{(n)} . \tag{3.8}$$

Here, P denotes the projection operator and $\underline{\hat{x}}$ is the HR image. Generally $\underline{\hat{x}}$ is the interpolated version of reference LR image, and it becomes the initial estimate. As an example, amplitude constraint set (3.9) with amplitude bounds of $\alpha=0$ and $\beta=255$ is given [29]. The projection P onto the amplitude constraint set C is shown in (3.10).

$$C=\{y(i,j):\alpha\le x(i,j)\le\beta\} \tag{3.9}$$

$$P[\hat{x}(i,j)]=\begin{Bmatrix} 0 & , & \hat{x}(i,j)<0 \\ \hat{x}(i,j) & , & 0<\hat{x}(i,j)<255 \\ 255 & , & \hat{x}(i,j)>255 \end{Bmatrix} \tag{3.10}$$

POCS procedure is an iterative method. The convergence can be provided by using closed convex sets [10].

Maximum Likelihood (ML) Estimation is a popular stochastic method. ML Estimation aims to maximize the conditional PDF of the observed data, given the original HR image $P(y|x)$.

By assuming the noise model of the observed images is zero mean white Gaussian with auto correlation matrix W^{-1} and after some mathematical steps, the ML is reduced to the weighted least squares (WLS) estimation [11]:

$$\begin{aligned}\underline{\hat{x}}_{ML} &= \arg\max_{\underline{x}} P(\underline{y}|\underline{x}) \\ &= \arg\max_{\underline{x}} \left\{ [\underline{y}-H\,\underline{x}]^T W [\underline{y}-H\,\underline{x}] \right\}.\end{aligned} \tag{3.11}$$

Differentiating the above formula with respect to $\underline{x}$ and equating to zero, $\underline{\hat{x}}_{ML}$ could be computed.

Another Stochastic SR image reconstruction method, also called Bayesian approach which resembles to ML Estimation, is Maximum a Posteriori Estimation (MAP) method. MAP maximizes the PDF of the original HR image, given the observed images $P(x \mid y)$.

$$\underline{\hat{x}} = \arg\max_{\underline{x}} P\left(\underline{x} \mid \underline{y}_1, \underline{y}_2, ..., \underline{y}_p\right) \tag{3.12}$$

By using the Bayesian rule, the above equation becomes,

$$\underline{\hat{x}} = \arg\max_{\underline{x}} P\left(\underline{y}_1, \underline{y}_2, ..., \underline{y}_p \mid \underline{x}\right) P(\underline{x}) \ . \tag{3.13}$$

MAP is a special case of ML, where the difference is the included *a-priori* information of the desired HR image. Since the inclusion of *a-priori* information is essential for the solution of ill posed problems, MAP estimation should be used in preference to ML estimation [6].

The detailed information about the Stochastic SR image Reconstruction with *a-priori* knowledge will be given in Chapter 5.

Generally the ML or MAP Estimators and the POCS method are used in the hybrid methods to construct a SR image. The aim is to combine the benefits of stochastic approaches and the set theoretic methods. Some application about hybrid methods can be found in [11, 12].

CHAPTER 4

BLUR MODELS AND BLUR ESTIMATION METHODS

While creating an image of a scene, it is required that the information of the observed data is useful and has more details. The detail information of the scene is included in the high frequency components of the image. Some effects cause blur degradation on the image. Blurring makes a low pass filtering operation on the image and suppresses the high frequency components. This also means losing of detail information of the scene.

Blurring effects reduce the bandwidth of the ideal HR image. It can be caused by the imperfect focusing of the camera lenses as shown in Figure 4.1. If there is a relative motion between the camera and the scene or if any object in the scene moves with respect to the camera, blurring exists on the movement direction. Also atmospheric conditions (temperature, exposure time, wind) cause blur on the image. These effects are named as the PSF of the sensors.

Blurring is a convolution operation in the spatial domain (4.1), (4.2) or a product operation in the frequency domain (4.3).

$$y(i, j) = h(k, l) \otimes x(i, j) \tag{4.1}$$

$$y(i, j) = \sum_{k=0}^{N-1} \sum_{l=0}^{M-1} h(k, l)\ x(i-k, j-l) \tag{4.2}$$

where y, h and x are the degraded image, blurring kernel and the original frame respectively. i, j, k and l are the indices of the images and the blurring kernel.

$$Y(w_1, w_2) = H(w_1, w_2) . X(w_1, w_2) \tag{4.3}$$

where Y, H and X are the Fourier transforms of the degraded image, blurring kernel and the original image frame respectively.

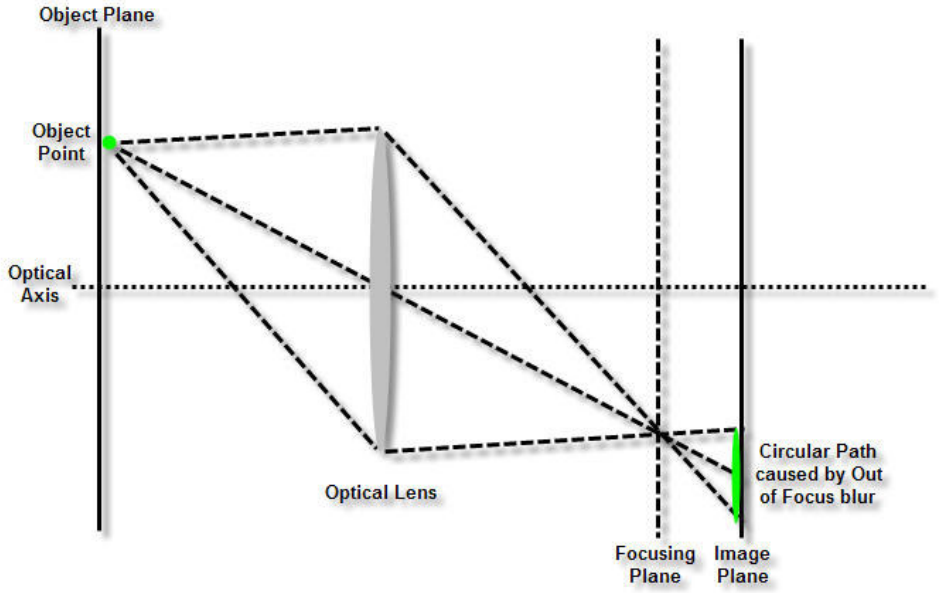

Figure 4.1 Formation of Out of Focus Blur.

The spatially continuous PSF $h(k,l)$ satisfies three constraints [13]:

- ✓ $h(k,l)$ takes non negative values only,
- ✓ when dealing with real valued images the PSF is real valued too,
- ✓ the sum of the blurring kernel values is equal to one (4.4), because the blurring degradation operation is an energy preserving transform.

$$\sum_{k=0}^{N-1}\sum_{l=0}^{M-1} h(k,l)=1 \tag{4.4}$$

The general PSF models can be categorized as follows:

- ✓ the Uniform Out of Focus Blur,
- ✓ the Motion Blur,
- ✓ Atmosphere (Gaussian Blur).

The Uniform Out of Focus blur is caused by the imperfect focusing of the camera. This type of blurring can affect the whole image or some parts of the image because of the distances of the objects in the scene. The spatially continuous PSF of the blurring kernel is given by:

$$d(x,y)=\begin{pmatrix} 0 & if\ \sqrt{x^2+y^2}>R \\ \dfrac{1}{\pi R^2} & if\ \sqrt{x^2+y^2}\le R \end{pmatrix} \tag{4.5}$$

where R is the diameter of the blurring kernel. In the discrete version boundary elements are not taken into account as shown in Figure 4.2. So the above formula can be expressed as:

$$d(x,y)=\begin{pmatrix} 0 & if\ \sqrt{x^2+y^2}>R \\ \dfrac{1}{C} & if\ \sqrt{x^2+y^2}\le R \end{pmatrix} \tag{4.6}$$

where C is a constant satisfying the condition in (4.4).

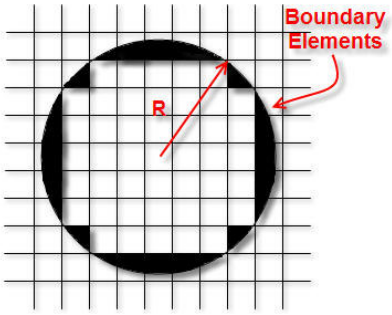

Figure 4.2 Boundary Elements of Blurring Kernel.

The relative motion between the imaging system and the scene or any object movement with respect to the camera in the scene cause the motion blur. This motion can be in the form of a translation, a rotation, a sudden change of scale, or some combinations of these [13]. The most important and generally used model is the linear motion blur. In this type of blurring, the motion is at a constant velocity and it makes an angle with the horizontal axis of the scene during the exposure time. The PSF kernel is given by:

$$d(i,j)=\begin{pmatrix} \frac{1}{L} & if\ \sqrt{i^2+j^2}\le L\ \ and\ \ \frac{vertical\ dist.}{horizontal\ dist.}=-\tan\varphi \\ 0 & elsewhere \end{pmatrix} \tag{4.7}$$

where L = *velocity* × *exposure time*, and φ is the angle between the motion and the horizontal axis of the image. A special case for $\varphi = 0$ of discrete version of this kernel is given by:

$$d(i,j)=\begin{pmatrix} \frac{1}{L^2} & if\ \ -\frac{L}{2}\le i,j\le\frac{L}{2} \\ 0 & elsewhere \end{pmatrix}. \tag{4.8}$$

The atmosphere turbulence blur relies on some factors such as wind, temperature, exposure time. Due to long term exposures, the PSF can be modeled as a Gaussian function.

$$d(i,j)=\left(C\,e^{-(i^2+j^2)/(2\sigma^2)}\right) \tag{4.9}$$

where σ is the variance of the Gaussian blur kernel and C is the constant satisfying the condition in (4.4).

Type and amount of the blurring kernel must be estimated / identified from the degraded observed image to achieve the best values of the high frequency components of the ideal HR image.

There exist two main blur estimation / identification approaches in the literature. The estimation of blur parameters and SR algorithm are handled jointly in the first approach. An example study for this type of approach can be found in [30]. The second approach, handled in this thesis study, is the identification of blur parameters out of the SR algorithm.

The general blur identification methods use the spectral zeros of the frequency domain values of the blurred images. But these methods could only identify a certain class of blurs.

M. E. Moghaddam has given a model to estimate out of focus blur in [14]. The proposed method aims to find the circular zero crossings of the logarithm spectrum of the degraded image. The absolute logarithm spectrum of the out of focus blurred images has circles that can be seen in Figure 4.3 (d) and (e). Moghaddam used Circular Hough Transform to estimate the diameter of these circles. The diameter of the circles has an inverse ratio with the original diameter of the blurring kernel as seen in Figure 4.3 (d) and (e). Then a formulation (4.10) shows the relation of the diameter of the zero crossing and the original diameter.

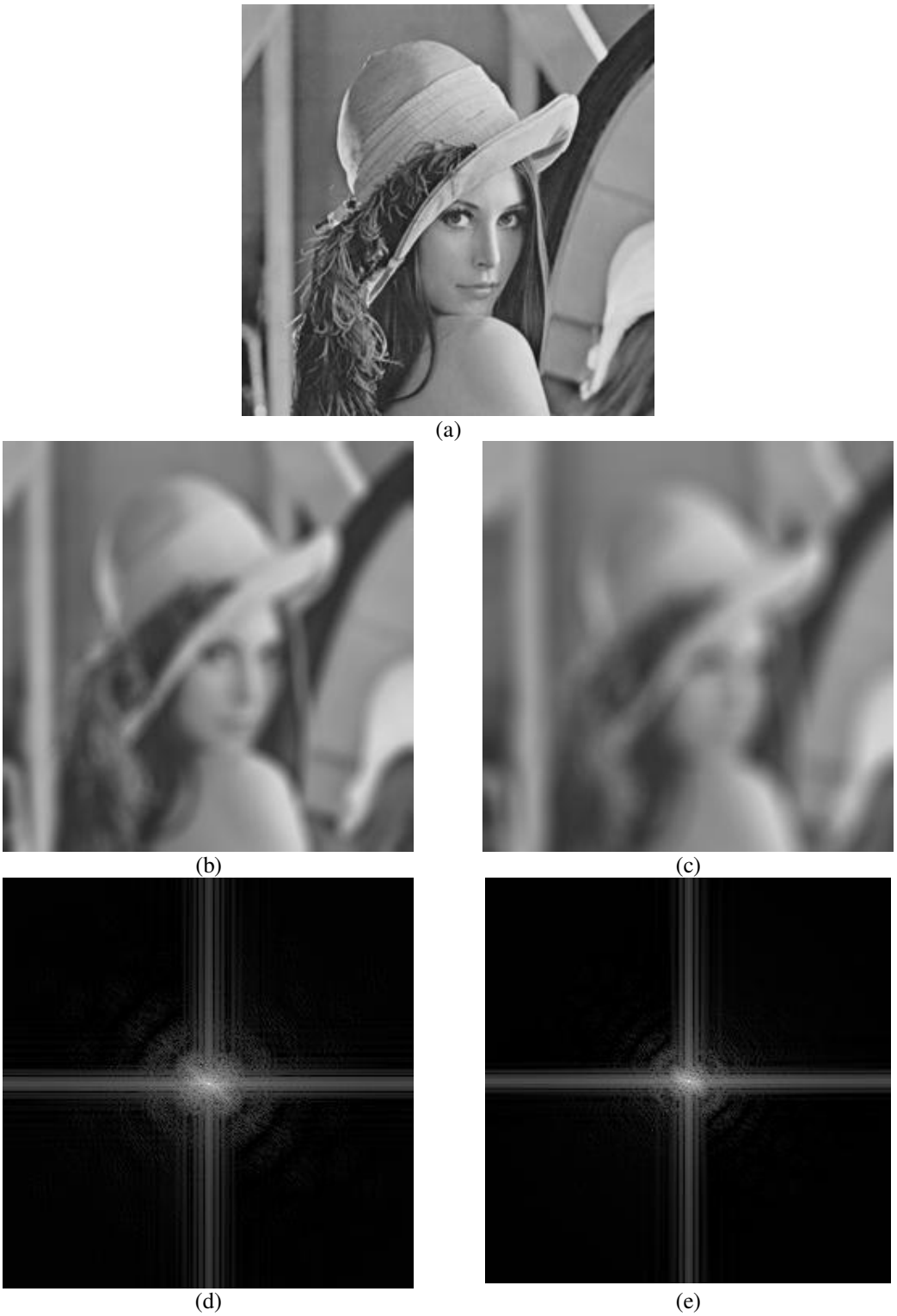

Figure 4.3 Spectrum Examples. The original image (a) is blurred with out of focus blurring kernels of 6 pixels radius (b) and 10 pixels radius (c). (d) and (e) are the corresponding spectrums of out of focus blurred images respectively.

$$R=\begin{cases} -0.0009R'^{3}+0.101R'^{2}-4.088R'+54.207 & if \quad R'>17 \\ -0.0012R'^{4}+0.1404R'^{3}-5.0373R'^{2}+70.623R'-319.241 & else \end{cases} \quad (4.10)$$

Shiqian Wu et.al. have used the cepstrum domain to identify blur parameters of out of focus blurred and motion blurred images [15]. The cepstrum domain is formulated as:

$$C(i,j)=F^{-1}\{\log|G(i,j)|\}. \quad (4.11)$$

where F^{-1} is the inverse Fourier transform operator, $G(i,j)$ is the Fourier Transform of the degraded image and $C(i,j)$ is the cepstrum of the degraded image. Because the logarithm of zero is negative infinite [15], it is also calculated as:

$$C(i,j)=F^{-1}\{\log|1+G(i,j)|\} \quad (4.12)$$

Corresponding cepstrums for out of focus blurred and motion blurred images are shown in Figure 4.4. As it is seen from Figure 4.4 (*f* and *g*) the spectral zero crossings or the spectral zeros give the parameters for blurring kernels. In the motion blur the zero crossings occur in the motion direction and with the length of the kernel size. In the out of focus blur a circle occurs and the radius of this formed circle is equal to double of the real blur kernel radius. To provide visibility of the normalized cepstrums, a mathematical operation is performed as:

$$Cepstrum\_Shown=\left(1-(1-Cepstrum)^{N}\right) \quad (4.13)$$

where *N* is the power coefficient as 10 or 20 that satisfies the visual improvement.

(a)

(b)

(c)

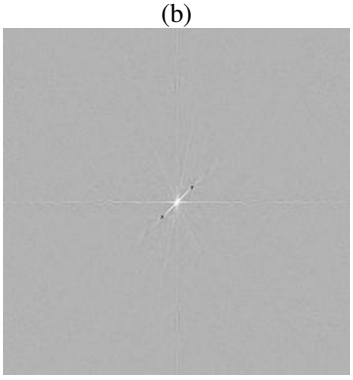

(d)

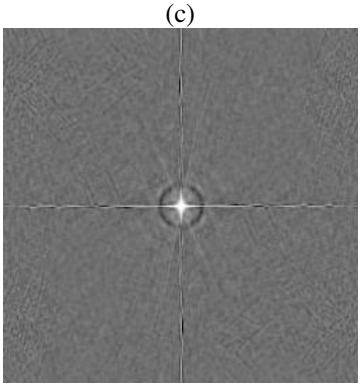

(e)

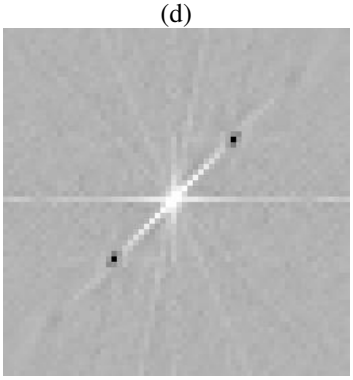

(f)

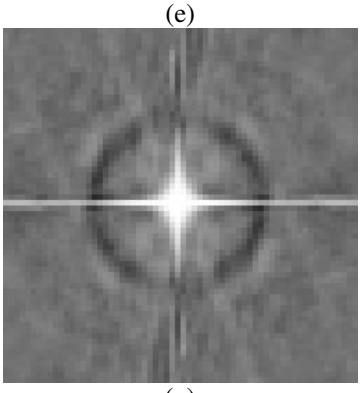

(g)

Figure 4.4 Cepstrum examples. The original image (a) is blurred with a motion blurring kernel of 11 pixels and an angle of 45 degrees (b). (a) is also blurred with an out of focus blurring kernel with a radius of 11 pixels (c). (d) and (e) are the corresponding cepstrums of motion blurred and out of focus blurred images respectively. (f) and (g) are the focused ceptrum centers respectively.

The above techniques can only be used for the PSFs of having spectral zeros. The Gaussian PSFs (Figure 4.5) do not have spectral zeros in frequency domain such as motion blur or out of focus blur [13, 16]. Therefore, the Gaussian PSF parameters could not be identified with the described techniques. The Gaussian PSFs have to be estimated from the degraded data. The general estimation techniques are the Auto Regressive Moving Average (ARMA) modeling [16 - 18] of the image and ML Estimation [13, 16].

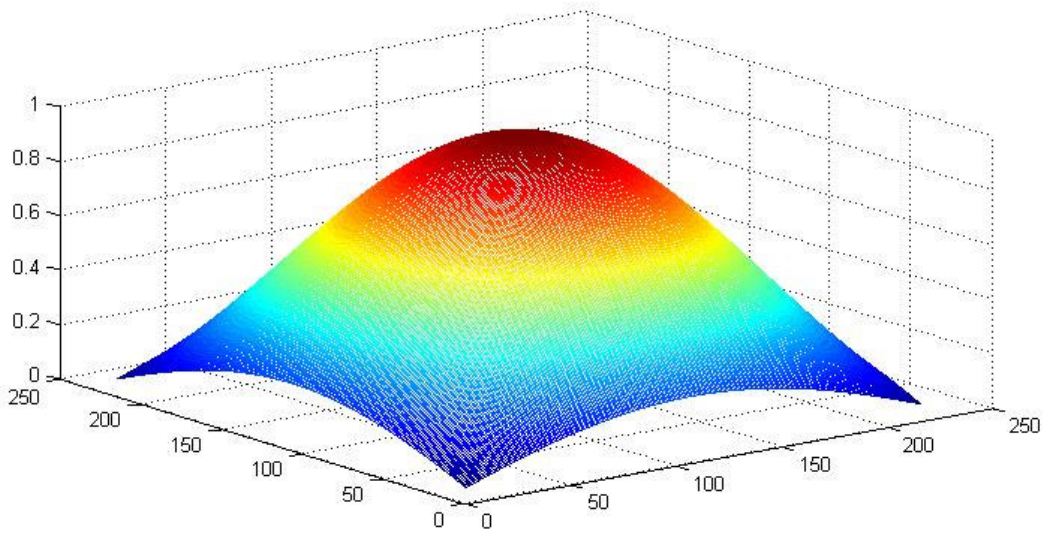

Figure 4.5 The frequency domain of Gaussian PSF.

In ARMA model, space models for the real image and the observed image are given as follows:

$$s(m,n)=\sum_{(k,l)\in R_{\oplus+}} c_{k,l}\, s(m-k,n-l)+w(m,n) \tag{4.14}$$

$$r(m,n)=\sum_{(i,j)\in R} h_{i,j}\, s(m-i,n-j)+v(m,n) \tag{4.15}$$

where

- ✓ s is the original HR frame,
- ✓ r is the observed noisy and blurred image,
- ✓ w and v are the independent zero mean Gaussian noise fields with variances σ_w^2 and σ_v^2 respectively,
- ✓ $c_{k,l}$'s are the nonsymmetrical half plane model support (4.16) parameters (Autoregressive (AR) part),
- ✓ $h_{i,j}$'s are the blurring parameters (Moving Average (MA) part),
- ✓ *m, n* are the image density indices; *i, j* are blur kernel indices and *k*, *l* are the half plane support indices.

$$R_{\oplus+} = \{(m-k,n-l) \,|\, (1 \le k < M, 0 \le l < M) \cup (-M \le k \le 0, 1 \le l \le M)\} \tag{4.16}$$

The relations (4.14, 4.15) are not suitable unless the original HR frame is known. Therefore $s(m,n)$ should be eliminated to get a useable model. Combining (4.14) and (4.15), interchanging the summations and substituting (4.15) back into the resulting equation [16], the model becomes:

$$\begin{aligned} r(m,n) = & \sum_{(k,l)\in R_{\oplus+}} c_{k,l}\, r(m-k,n-l) \\ & + \sum_{(i,j)\in R} h_{i,j}\, w(m-i,n-j) + v(m,n) - \sum_{(k,l)\in R_{\oplus+}} c_{k,l}\, v(m-k,n-l) \end{aligned} \tag{4.17}$$

Moreover, if (4.18) is defined, the equation (4.17) turns into (4.19).

$$x(m,n) = r(m,n) - v(m,n) \tag{4.18}$$

$$x(m,n) = \sum_{(k,l)\in R_{\oplus+}} c_{k,l}\, x(m-k,n-l) + \sum_{(i,j)\in R} h_{i,j}\, w(m-i,n-j). \tag{4.19}$$

Given the representation of (4.19), a likelihood function can be defined as:

$$L(\theta)=\log\ p\left(x(m,n)\,|\,\theta\right) \tag{4.20}$$

where $\theta=[\{c_{k,l}\},\{h^{*}_{-+}(i,j)\}]$ and $h^{*}_{-+}(i,j)$ are the quarter plane factors described in (4.22) and (4.23) [16]. After some steps explained in [16] by Tekalp et.al., maximizing the likelihood function turns into minimizing the below function:

$$\tilde{L}(\theta)=\frac{1}{N}\sum_{W} w^{2}(m,n) \tag{4.21}$$

where N is the number of observations.

$$h(i,j)=h_{-+}(i,j)*h_{++}(i,j)*h_{--}(i,j)*h_{+-}(i,j) \tag{4.22}$$

$$h_{-+}(i,j)=h_{++}(-i,+j)=h_{--}(+i,-j)=h_{+-}(-i,-j) \tag{4.23}$$

where Figure 4.6 shows the quarter plane factors and their direction of recursion.

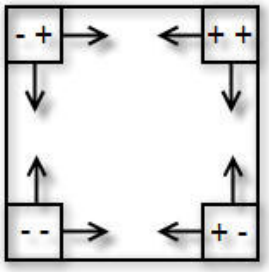

Figure 4.6 Quarter plane factors and their direction of recursion.

For computing the equation (4.21), $x(m,n)$ is passed through the model transfer function defined as:

$$H_F(z_1,z_2)=\frac{1-C(z_1,z_2)}{H(z_1,z_2)} \tag{4.24}$$

where H_F, C and H represents the frequency domain values of transfer function, half plane support parameters and blur kernel respectively.

By applying the quarter plane factors (4.24) turns into:

$$H_F(z_1,z_2)=\frac{1-C(z_1,z_2)}{H_{-+}(z_1,z_2)H_{++}(z_1,z_2)H_{--}(z_1,z_2)H_{+-}(z_1,z_2)} \tag{4.25}$$

Another method for Gaussian PSF estimation based on Kurtosis minimization is given by Dalong et.al. in [19]. The Kurtosis is a measure of the peakedness of the probability distribution of a real-valued random variable and is defined as the fourth central moment (4.26) of that random variable. The normal distribution has a kurtosis value of three and named as mesokurtic. Kurtosis values smaller than three are named platycurtic and the values above three are called leptokurtic.

$$Kurtosis=\frac{E\left((x-\mu)^4\right)}{\sigma^4} \tag{4.26}$$

where σ is the standard deviation, μ is the mean value and x is the random variable.

Dalong et.al. restored the blurred, noisy images by wiener filter using different variances and different sized Gaussian PSF blurring kernels. The kurtosis value of the restored image is used as a measurement parameter. Because the larger kurtosis

in a platycurtic distribution means a smoother data [19], the PSF that satisfies the minimum kurtosis value is accepted as the real PSF kernel. They compared the results with Peak Signal Noise Ratio (PSNR) values of the restored images and showed that the max PSNR gives the minimum kurtosis value.

Also some edge based blur identification methods for Gaussian PSFs are discussed in [20, 21]. H.Hu and G.de Haan proposed a method that finds the Gaussian blur radius by using the differences between the observed image and its reblurred versions [20]. An edge localization and derivative procedure is given for Gaussian blur identification by Ming Chao Chiang and Terrence E. Boult [21].

CHAPTER 5

EXPERIMENTAL STUDIES

The studies continued in this thesis can be categorized into two main titles: estimation of the blur parameters and the SR reconstruction studies. In the SR study part, one of the well known SR image reconstruction methods, the stochastic method with *a priori* knowledge, is handled. In the blur estimation part, the identification performances of different methods for different blur models are discussed under noiseless and noisy conditions. In the rest of this section the experimental studies and the results are given.

5.1. Stochastic Image Reconstruction Method with *a Priori* Knowledge – Maximum a Posteriori Method

In statistics, the method of MAP estimation can be used to obtain a point estimate of an unobserved quantity on the basis of empirical data. MAP employs an augmented optimization objective which incorporates a prior distribution over the quantity one wants to estimate [31].

MAP estimation technique is used to obtain the HR image x given the ensemble of LR images. The estimation of the HR image from LR ones is given as:

$$\underline{\hat{x}} = \arg\max_{\underline{x}} P(\underline{x} | \underline{y_1}, \underline{y_2}, ..., \underline{y_p}) . \tag{5.1}$$

From Bayes' rule, this can be written as:

$$\underline{\hat{x}} = \arg\max_{\underline{x}} \frac{P(\underline{y_1}, \underline{y_2}, ..., \underline{y_p} | \underline{x}) P(\underline{x})}{P(\underline{y_1}, \underline{y_2}, ..., \underline{y_p})} \tag{5.2}$$

Since the denominator is not a function of $\hat{\underline{x}}$, above equation becomes:

$$\hat{\underline{x}} = \arg\max_{\underline{x}} P(\underline{y_1}, \underline{y_2}, ..., \underline{y_p} | \underline{x}) P(\underline{x}). \tag{5.3}$$

Taking the log of posterior probability,

$$\hat{\underline{x}} = \arg\max_{\underline{x}} [\log P(\underline{y_1}, \underline{y_2}, ..., \underline{y_p} | \underline{x}) + \log\ P(\underline{x})]. \tag{5.4}$$

Hence, we need to specify the conditional density $P(\underline{y_1}, \underline{y_2}, ..., \underline{y_p} | \underline{x})$ and the prior image density $P(\underline{x})$. $P(\underline{x})$ is used as regularization term and it can be defined by different models. Because small amount of noise will result in large perturbations, considering regularization in SR algorithm as a means for picking a stable solution is very useful [22].

Since the noises (n_i's) are independent,

$$\hat{\underline{x}} = \arg\max_{\underline{x}} [\log \prod_{i=1}^{p} P(\underline{y_i} | \underline{x}) + \log\ P(\underline{x})], \tag{5.5}$$

$$\hat{\underline{x}} = \arg\max_{\underline{x}} [\sum_{i=1}^{p} \log P(\underline{y_i} | \underline{x}) + \log\ P(\underline{x})]. \tag{5.6}$$

Since the noise is assumed to be i.i.d. Gaussian,

$$P(\underline{y_i} | \underline{x}) = \left[\sum_{i=1}^{p} \log \frac{1}{\left(2\pi\sigma_\eta^2\right)^{\frac{MN}{2}}} \times \exp\left\{ - \frac{\left\| \underline{y_i} - H_i D \underline{x} \right\|^2}{2\sigma_\eta^2} \right\} \right], \tag{5.7}$$

$$P(\underline{y}_i|\underline{x}) = -\sum_{i=1}^{p} \frac{\left\| \underline{y}_i - H_i D\underline{x} \right\|^2}{2\sigma_n^2} - \frac{MN}{2}\log\left(2\pi\sigma_n^2\right). \tag{5.8}$$

Eliminating the constants, the conditional density becomes

$$P(\underline{y}_i|\underline{x}) = -\sum_{i=1}^{p} \left\| \underline{y}_i - H_i D\underline{x} \right\|^2 . \tag{5.9}$$

Substituting (5.9) into (5.6), the final cost function becomes:

$$\underline{\hat{x}} = \arg\max_{\underline{x}} \left[\sum_{i=1}^{p} - \left\| \underline{y}_i - H_i D\underline{x} \right\|^2 - regularization\ term \right] \tag{5.10}$$

or

$$\underline{\hat{x}} = \arg\min_{x} \left[\sum_{i=1}^{p} \left\| \underline{y}_i - H_i D\underline{x} \right\|^2 + regularization\ term \right]. \tag{5.11}$$

The above cost function resembles the given cost function form in deterministic method (3.3) with the difference of regularization term. The regularization operator C is generally a high pass filter in deterministic method, but in MAP method the regularization term depends on PDF of solution $\underline{x}$, $\log P(\underline{x})$.

Sina Farsiu et.al. have used L1 Norm (5.12) approach instead of L2 Norm as data fidelity term for general purpose, because L2 Norm is only optimal for the case of Gaussian noise [22, 26].

$$\underline{\hat{x}} = \arg\min_{\underline{z}} \left[\sum_{i=1}^{p} \left\| \underline{y}_i - H_i D\underline{x} \right\|_1 + regularization\ term \right] \tag{5.12}$$

D. Rajan and S. Chaudhuri have given a Markov Random Field (MRF) based prior model with Gibbs density function in [23, 24] as:

$$P(\underline{x})=\frac{1}{Z}\exp\left\{-\sum_{c\in C}V_c(\underline{x})\right\}, \tag{5.13}$$

where Z is a normalizing constant known as the partition function, $V_c(\ )$ is the clique potential and C is the set of all cliques in the image. Cliques depend on the neighborhood of the pixels shown in Figure 5.1.

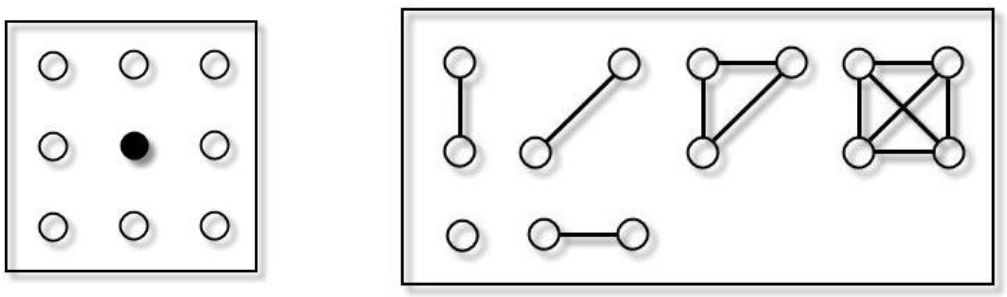

(a) (b)

Figure 5.1 Eight neighbors of the pixel (a) and the possible clique combinations (b).

Different cost functions can be written by using various clique combinations. As an example, a quadratic cost which is a function of finite difference approximations of first order derivative at each pixel location can be shown as follows:

$$\sum_{c\in C}V_c(x)=\lambda\sum_{k=1}^{M}\sum_{l=1}^{N}\left[\left(x_{k,l}-x_{k,l-1}\right)^2+\left(x_{k,l}-x_{k,l+1}\right)^2+\left(x_{k,l}-x_{k-1,l}\right)^2+\left(x_{k,l}-x_{k+1,l}\right)^2\right] \tag{5.14}$$

where λ is a tuning (regularization) parameter.

Sina Farsiu et.al. have given different regularization term models in [22, 26], which are

- ✓ Tikhonov,
- ✓ Total Variation (TV),
- ✓ Bilateral Total Variation (BTV).

The Tikhonov regularization term is defined as:

$$\mathrm{T}(x)=\|\Gamma x\|_2^2 \tag{5.15}$$

where the kernel is

$$\Gamma_{\mathrm{ker}nel}=\frac{1}{8}\begin{bmatrix}1 & 1 & 1\\ 1 & -8 & 1\\ 1 & 1 & 1\end{bmatrix}. \tag{5.16}$$

TV Prior is an edge preserving regularization term model and defined as:

$$TV(x)=\|\nabla x\|_1 \tag{5.17}$$

where ∇ is the gradient operator. The mathematical form is:

$$TV(x)=\lambda\sum_{l=-P}^{P}\sum_{m=0}^{P}\alpha^{|m|+|l|}\left\|x-S_x^l S_y^m x\right\|_1 \quad where\ l+m\geq 1\ and\ P=1 \tag{5.18}$$

where S_x^l and S_y^m shift x in horizontal and vertical directions by *l* and *m* pixels. λ is the regularization parameter and α is the scalar weight of the derivatives. The BTV regularization resembles TV regularization. The only difference is $(P>1)$.

The regularization parameters in (5.14) and (5.18) dictate the strength with which the regularization term is enforced [26]. Assigning the value of λ can be done by visual inspection or automatically by using some methods as Generalized Cross Validation or L-curve. The scalar weight α in (5.18) is assigned between zero and one, $0 < \alpha < 1$, to satisfy a spatially decaying effect to the summation [26].

Our aim now reduces to minimizing the cost function in (5.11). The generally used minimization procedure is the gradient descent optimization which is an iterative procedure. Thus the estimated image $\underline{\hat{x}}$ of the $(n+1)^{th}$ iteration is written as:

$$\underline{\hat{x}}_{n+1} = \underline{\hat{x}}_n - \beta\left[\sum_{i=1}^{p} H_i^T D_i^T (D_k H_k \underline{\hat{x}}_n - \underline{y}_i) + \lambda \partial(\textit{regularization term}) / \partial \underline{x}\right]. \tag{5.19}$$

The regularization terms mentioned above are used with L1 and L2 norms. The gradients of all different of regularization terms are given below.

Gradient of L1 Norm and MRF based regularization term:

$$\underline{\hat{x}}_{(n+1)} = \underline{\hat{x}}_{(n)} - \beta\left[\begin{array}{l} \dfrac{1}{\sigma_\eta^2}\displaystyle\sum_{i=1}^{p} D^T H_i^T \, sign(H_i D \underline{\hat{x}}_{(n)} - \underline{y_i}) \; + \\ \qquad 2\lambda \displaystyle\sum_{k=1}^{M}\sum_{l=1}^{N} (4\underline{\hat{x}}_{(n)k,l} - \underline{\hat{x}}_{(n)k,l-1} - \underline{\hat{x}}_{(n)k,l+1} - \underline{\hat{x}}_{(n)k-1,l} - \underline{\hat{x}}_{(n)k+1,l}) \end{array}\right] \tag{5.20}$$

Gradient of L1 Norm and Tikhonov regularization term:

$$\underline{\hat{x}}_{n+1} = \underline{\hat{x}}_n - \beta\left[\sum_{k=1}^{p} H_k^T D_k^T sign(D_k H_k \underline{\hat{x}}_n - \underline{y}_k) + \lambda \Gamma^T (\Gamma \underline{\hat{x}}_n)\right] \tag{5.21}$$

Gradient of L1 Norm and TV regularization term:

$$\underline{\hat{x}}_{n+1} = \underline{\hat{x}}_n - \beta \left[\sum_{k=1}^{p} H_k^T D_k^T sign(D_k H_k \underline{\hat{x}}_n - \underline{y}_k) + \lambda \sum_{l=-1}^{1} \sum_{m=0}^{1} \alpha^{|m|+|l|} \left(I - S_x^{-m} S_y^{-l} \right) sign(\underline{\hat{x}}_n - S_x^l S_y^m \underline{\hat{x}}_n) \right] \tag{5.22}$$

Gradient of L1 Norm and BTV regularization term:

$$\underline{\hat{x}}_{n+1} = \underline{\hat{x}}_n - \beta \left[\sum_{k=1}^{p} H_k^T D_k^T sign(D_k H_k \underline{\hat{x}}_n - \underline{y}_k) + \lambda \sum_{l=-2}^{2} \sum_{m=0}^{2} \alpha^{|m|+|l|} \left(I - S_x^{-m} S_y^{-l} \right) sign(\underline{\hat{x}}_n - S_x^l S_y^m \underline{\hat{x}}_n) \right] \tag{5.23}$$

Gradient of L2 Norm and MRF based regularization term:

$$\underline{\hat{x}}_{(n+1)} = \underline{\hat{x}}_{(n)} - \beta \left[\frac{1}{\sigma_\eta^2} \sum_{i=1}^{p} D^T H_i^T (H_i D \underline{\hat{x}}_{(n)} - \underline{y}_i) + 2\lambda \sum_{k=1}^{M} \sum_{l=1}^{N} (4 \underline{\hat{x}}_{(n)k,l} - \underline{\hat{x}}_{(n)k,l-1} - \underline{\hat{x}}_{(n)k,l+1} - \underline{\hat{x}}_{(n)k-1,l} - \underline{\hat{x}}_{(n)k+1,l}) \right] \tag{5.24}$$

Gradient of L2 Norm and Tikhonov regularization term:

$$\underline{\hat{x}}_{n+1} = \underline{\hat{x}}_n - \beta \left[\sum_{k=1}^{p} H_k^T D_k^T (D_k H_k \underline{\hat{x}}_n - \underline{y}_k) + \lambda \Gamma^T (\Gamma \underline{\hat{x}}_n) \right] \tag{5.25}$$

Gradient of L2 Norm and TV regularization term:

$$\underline{\hat{x}}_{n+1} = \underline{\hat{x}}_n - \beta \left[\sum_{k=1}^{p} H_k^T D_k^T (D_k H_k \underline{\hat{x}}_n - \underline{y}_k) + \lambda \sum_{l=-1}^{1} \sum_{m=0}^{1} \alpha^{|m|+|l|} \left(I - S_x^{-m} S_y^{-l} \right) sign(\underline{\hat{x}}_n - S_x^l S_y^m \underline{\hat{x}}_n) \right] \tag{5.26}$$

Gradient of L2 Norm and BTV regularization term:

$$\underline{\hat{x}}_{n+1} = \underline{\hat{x}}_n - \beta \left[\sum_{=1}^{p} \begin{array}{l} H_k^T D_k^T (D_k H_k \underline{\hat{x}}_n - \underline{y}_k) + \\ \lambda \sum_{l=-2}^{2} \sum_{m=0}^{2} \alpha^{|m|+|l|} \left(I - S_x^{-m} S_y^{-l} \right) sign(\underline{\hat{x}}_n - S_x^l S_y^m \underline{\hat{x}}_n) \end{array} \right] \tag{5.27}$$

For evaluating the performances of the given cost functions above different LR images are created from the images given in Figure 5.2. The HR images are convolved by blurring kernels sized 7×7 pixels with variances (0.3, 0.5, 0.7, 0.9 and 1.1) then the dimensions are decreased by a factor of two and a white Gaussian noise with a variance of 5.0 is added. As an example, the original frame and the corresponding LR frames of Cameraman image are shown in Figure 5.3.

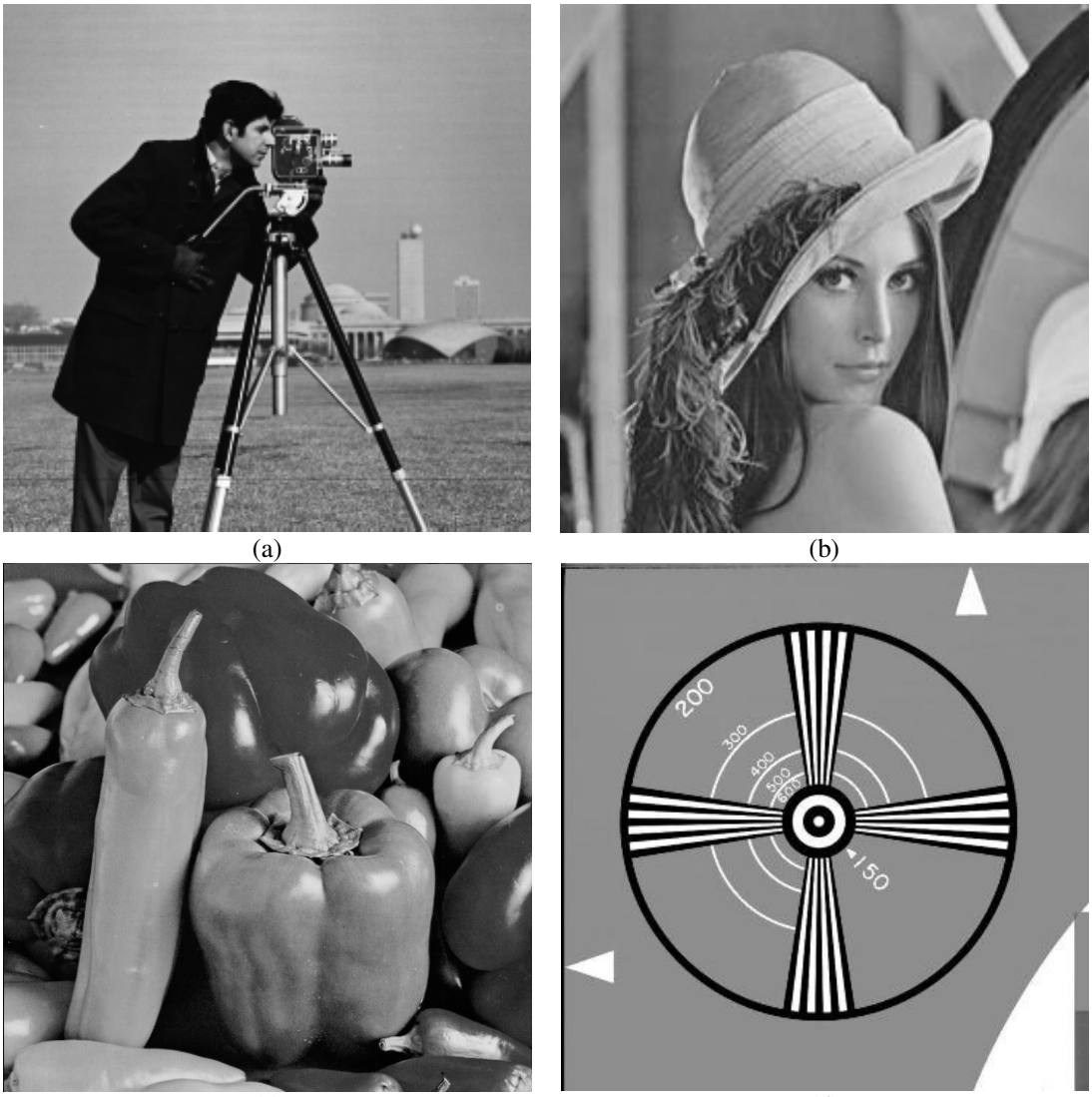

(a) (b)

(c) (d)

Figure 5.2 The used test images. Cameraman (a), Lena (b), Peppers (c) and Eia (d).

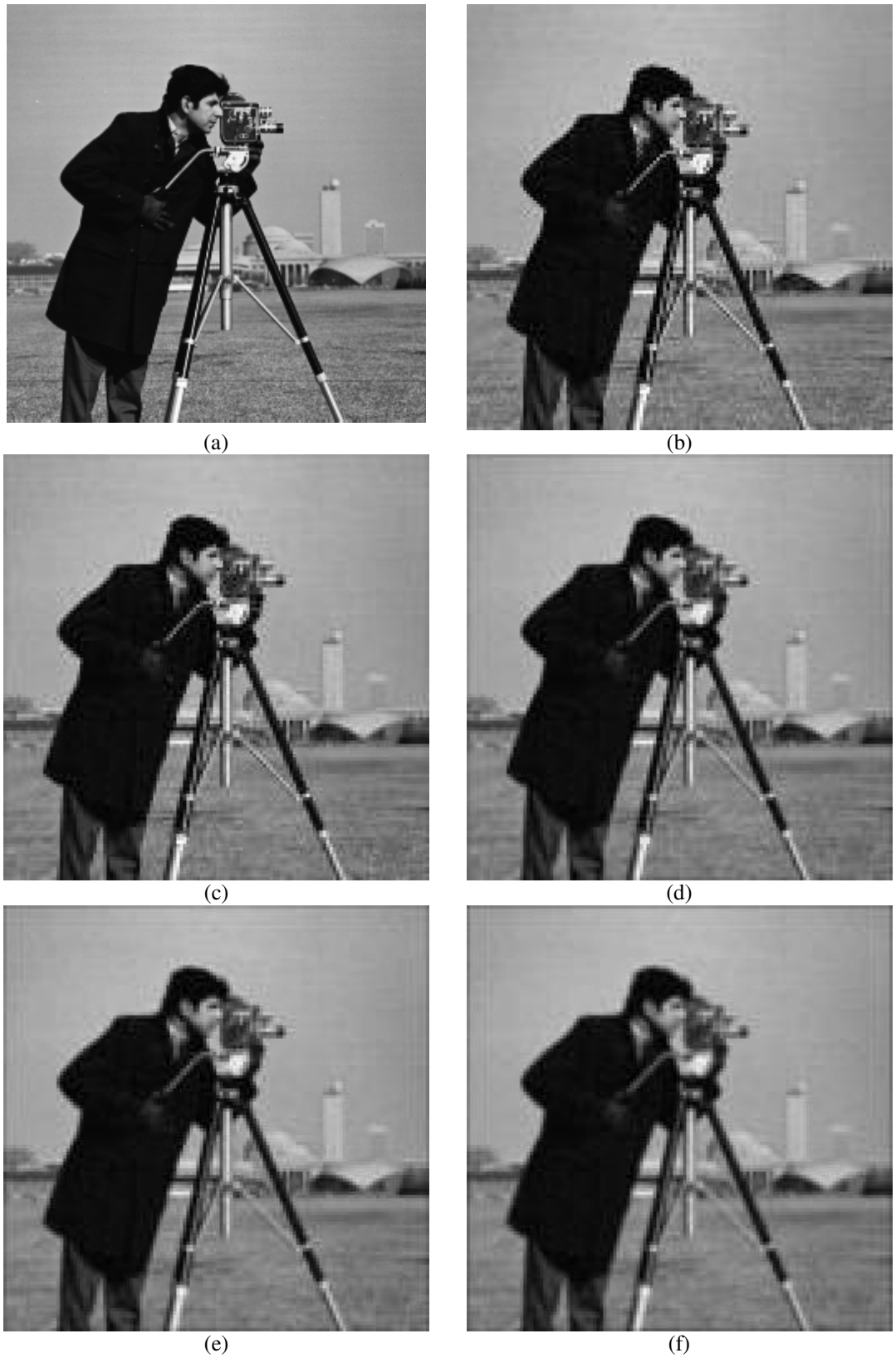

(a) (b) (c) (d) (e) (f)

Figure 5.3 The original image (a) and LR frames blurred by different variance Gaussian kernels (0.3, 0.5, 0.7, 0.9 and 1.1 respectively) and added noise (b - f).

The regularization parameter λ is chosen as 0.06 for MRF based regularization term and 0.4 for other regularization terms. The scalar weight α is assigned as 0.6 for TV and BTV regularization terms. The initial estimate of the image $\hat{x}$ is chosen as the bilinear interpolation of the least degraded LR image frame. Mean Square Error (MSE) (5.28) and PSNR (5.29) criterions are used for the performance measurement.

$$MSE = \frac{\sum_{i=1}^{M}\sum_{j=1}^{N}\left(\underline{\hat{x}}(i,\ j) - x(i,\ j)\right)^2}{\sum_{i=1}^{M}\sum_{j=1}^{N}\left(x(i,\ j)\right)^2} \tag{5.28}$$

$$PSNR = 10\log_{10}\frac{\sum_{i=1}^{M}\sum_{j=1}^{N}255^2}{\sum_{i=1}^{M}\sum_{j=1}^{N}\left(x(i,j) - \underline{\hat{x}}(i,j)\right)^2} \tag{5.29}$$

Table 5.1 shows the results of reconstruction approaches for the test images given in Figure 5.2. In the first column the applied stochastic approaches (5.20 – 5.27) are given. Estimated Image results are put as a row at the bottom of each method to make compare easy. "Iter. No" shows the iteration number of the methods. All of the iterations of "L1 Norm & Tikhonov Regularization" and some of the iterations of "L2 Norm & Tikhonov Regularization" approaches are stopped after a level, because the results get worse after an amount of iterations. The stopped iteration result areas are marked with (***). The best results are reached with "L1 Norm & TV Regularization" and "L1 Norm & BTV Regularization", these areas are written bold and italic.

Table 5.1 Results of the reconstruction approaches.

IMAGE		LENA		CAMERAMAN		PEPPERS		EIA	
METHOD	Iter. No	MSE	PSNR	MSE	PSNR	MSE	PSNR	MSE	PSNR
L1 Norm & MRF Based Regularization	10	0,0037	29,5037	0,0085	26,1979	0,0079	26,7042	0,0128	23,6505
	35	0,0039	29,296	0,008	26,4979	0,0072	27,0932	0,0101	24,6754
	50	0,004	29,1765	0,0078	26,5756	0,0071	27,1537	0,0095	24,9303
	100	0,0046	28,5808	0,008	26,508	0,007	27,2222	0,0084	25,453
Estimated Image		0,0053	25,7405	0,0107	25,2159	0,0118	24,9702	0,0177	22,24
L2 Norm & MRF Based Regularization	10	0,008	26,2087	0,0135	24,2142	0,014	24,2131	0,0138	23,3016
	35	0,0065	27,0829	0,012	24,7282	0,0118	24,9692	0,0141	23,2295
	50	0,0053	28,0073	0,0104	25,3598	0,0094	25,9719	0,0117	24,0228
	100	0,0053	27,972	0,0103	25,3714	0,0093	25,9929	0,0118	23,9981
Estimated Image		0,0053	25,7405	0,0107	25,2159	0,0123	24,9702	0,0176	22,24
L1 Norm & TV Regularization	10	0,0036	29,6625	0,0084	26,2614	0,0077	26,8055	0,0126	23,6912
	35	0,0033	30,017	0,0073	26,8596	0,0068	27,7151	0,0093	25,0467
	50	***0,0033***	***30,044***	0,0071	26,9737	0,0066	27,3556	0,0084	25,4473
	100	0,0034	29,8829	***0,0069***	***27,1253***	***0,0063***	***27,4835***	***0,0067***	***26,481***
Estimated Image		0,0053	25,7405	0,0107	25,2159	0,0118	24,9702	0,0177	22,24
L2 Norm & TV Regularization	10	0,0056	27,784	0,011	25,1119	0,0113	25,1723	0,0183	22,0789
	35	0,0062	27,2729	0,0116	24,8733	0,0104	25,5352	0,0205	21,6029
	50	0,0066	27,0415	0,0119	24,7507	0,01	25,6801	0,0208	21,3181
	100	0,0074	26,5256	0,0126	24,4945	0,0094	25,9626	0,0261	20,5503
Estimated Image		0,0053	25,7405	0,0107	25,2159	0,0118	24,9702	0,0177	22,24
L1 Norm & BTV Regularization	10	0,0036	29,6287	0,0085	26,212	0,0076	26,8812	0,0129	23,5919
	35	0,0033	30,0218	0,0073	26,8615	0,0065	27,5317	0,0092	25,0668
	50	***0,0033***	***30,0303***	0,0072	26,9275	0,0063	27,6644	0,0083	25,5241
	100	0,0034	29,9571	***0,007***	***27,0501***	***0,006***	***27,8861***	***0,0067***	***26,4619***
Estimated Image		0,0053	25,7405	0,0107	25,2159	0,0118	24,9702	0,0177	22,24
L2 Norm & BTV Regularization	10	0,0064	27,2	0,0118	24,7918	0,0116	25,055	0,0183	22,0789
	35	0,0087	25,8141	0,0143	23,9589	0,0116	24,0306	0,0205	21,6029
	50	0,0098	25,3169	0,0154	23,6336	0,0118	24,9653	0,0218	21,3181
	100	0,0124	24,3026	0,018	22,9606	0,0124	24,7474	0,0261	20,5503
Estimated Image		0,0053	25,7405	0,0107	25,2159	0,0118	24,9702	0,0177	22,24
L1 Norm & Tikhonov Regularization	10	0,0043	28,8943	0,0089	26,0384	0,0084	26,4488	0,0126	23,7194
	35	0,0569	17,6809	0,0628	17,5341	0,0328	20,5344	0,0896	15,1894
	50	***	***	***	***	***	***	***	***
	100	***	***	***	***	***	***	***	***
Estimated		0,0053	25,7405	0,0107	25,2159	0,0118	24,9702	0,0177	22,24
L2 Norm & Tikhonov Regularization	10	0,0056	27,784	0,0095	25,7311	0,011	25,2493	0,0146	23,0683
	35	0,0062	27,2729	0,0668	17,2691	0,0296	20,9781	0,0831	15,5131
	50	0,0066	27,0415	***	***	***	***	***	***
	100	0,0074	26,5256	***	***	***	***	***	***
Estimated Image		0,0053	25,7405	0,0107	25,2159	0,0118	24,9702	0,0177	22,24

In Chapter 2 the image formation model was given as matrix forms. But these matrices can be interpreted as direct image operators such as shift, blur and decimation [22]. The computational complexity and the hardware requirement reduce due to using the direct image operators. An example application schema of "L1 Norm & TV Regularization" (5.22) and "L1 Norm & BTV Regularization" (5.23) is shown below.

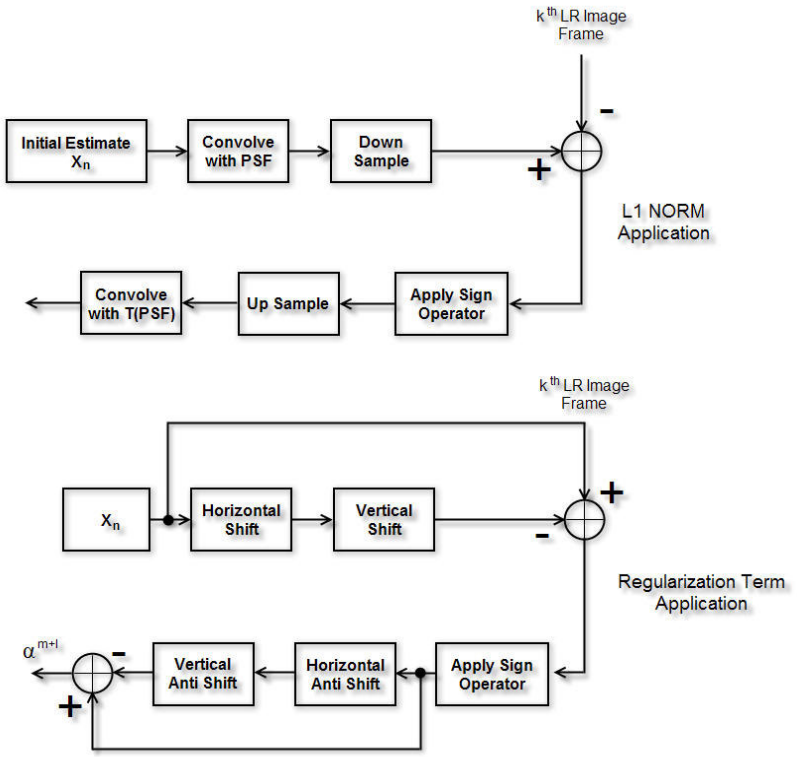

Figure 5.4 Block Diagram of direct image operator applications.

The initial estimates and the superresolved images are shown in the following figures.

(a) MSE = 0.0107 PSNR = 25.2159 (b) MSE = 0.0069 PSNR = 27.1253

(c) MSE = 0.0053 PSNR = 25.7405 (d) MSE = 0.0033 PSNR = 30.0333

Figure 5.5 The bilinear interpolated initial estimates (a, c) from LR frames and SR frames (b, d) of the test images.

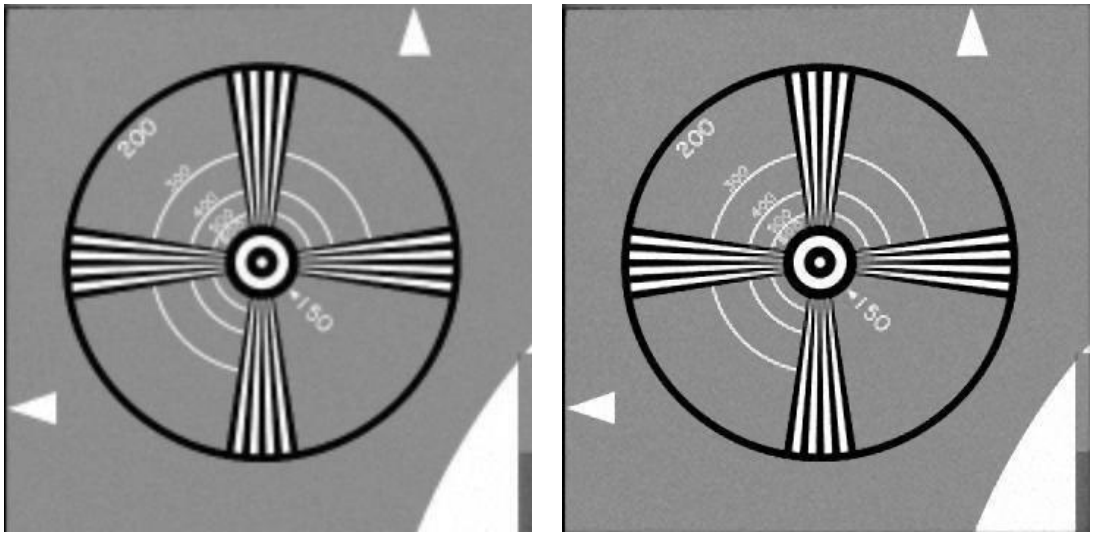

(a) MSE = 0.0177 PSNR = 22.2400 (b) MSE = 0.0067 PSNR = 26.4679

(c) MSE = 0.0118 PSNR = 24.9702 (d) MSE = 0.0063 PSNR = 27.4835

Figure 5.6 The bilinear interpolated initial estimates (a, c) from LR frames and SR frames (b, d) of the test images.

5.2. Blur Identification

Because SR image reconstruction is an ill posed inverse problem, the degradation models must be known or identified from the observations while achieving a superresolved image from a sequence of degraded images. Blur is one of the degradation operators. As mentioned before, the general encountered blur models are:

- ✓ Out of Focus Blur,
- ✓ Motion Blur,
- ✓ Gaussian Blur.

In this part, the identification methods of mentioned blur types are applied and the performance will be discussed.

5.2.1. Out of Focus Blur Identification

For the identification of out of focus blur, the logarithm spectrum approach [14] and the cepstrum approach [15] are tried with noiseless and noisy observations for different sized blur kernels. The methods are tried on different sized images: Lena, Eia, Peppers, and Cameraman shown in Figure 5.2. All of the images are convolved with the same blurring kernels and the results are compared.

As seen from the Figures 5.7 and 5.8, the first spectral zeros occur at the 10^{th} pixel of the diagonal from the center for the noiseless and noisy out of focus blurred Lena images with a blurring radius of 11 pixels. Table 5.2 shows the first spectral zeros of the images for different blur radius values.

Table 5.2 First spectral zeros of out of focus blurred images (Spectrum Method).

Image	Lena		Eia		Peppers		Cameraman	
Blur Radius	N.less	Noisy	N.less	Noisy	N.less	Noisy	N.less	Noisy
5 pixels	25^{th} p	24^{th} p	32^{nd} p	36^{th} p	---	---	22^{nd} p	25^{th} p
7 pixels	16^{th} p	19^{th} p	21^{rst} p	21^{rst} p	---	---	16^{th} p	18^{th} p
11 pixels	10^{th} p	10^{th} p	10^{th} p	11^{th} p	---	---	11^{th} p	9^{th} p

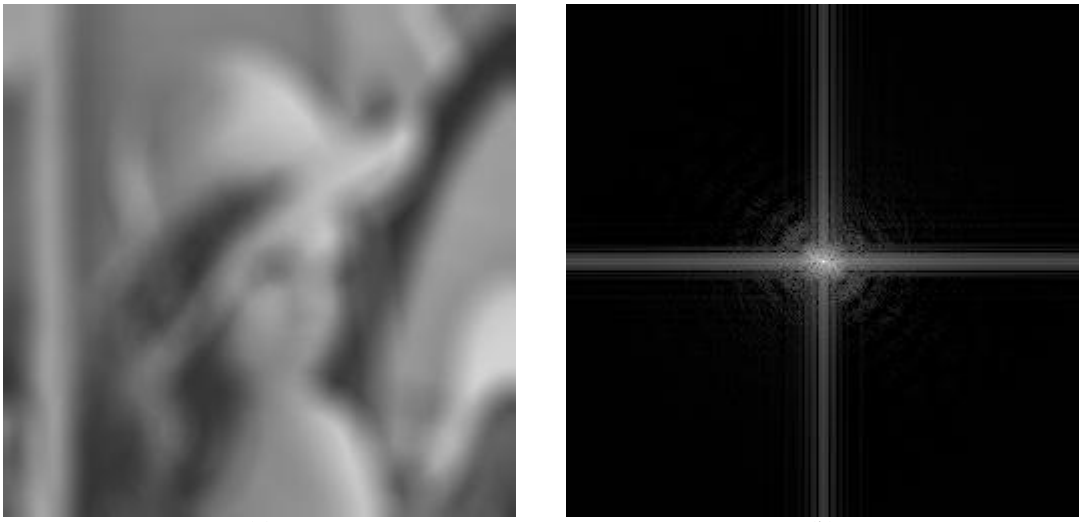

(a) (b)

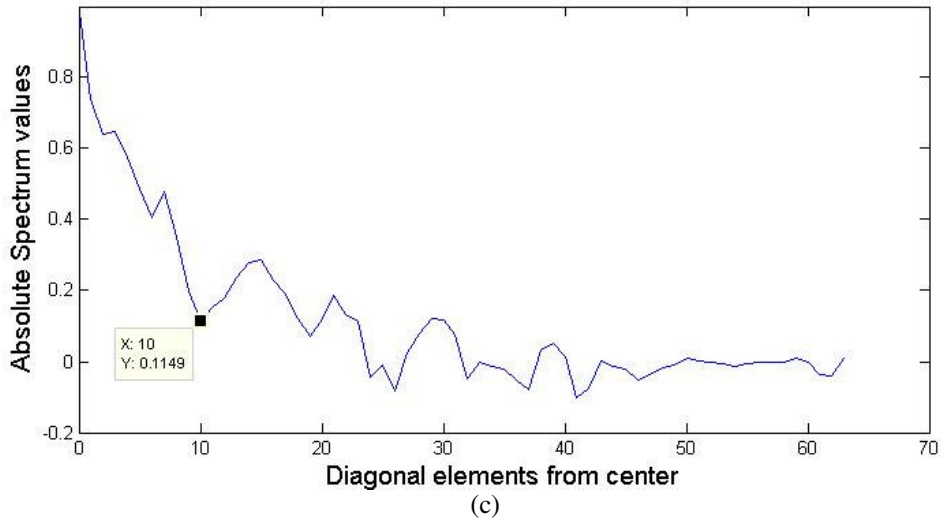

(c)

Figure 5.7 The logarithm spectrum of out of focus blurred image (a) is shown in (b). (c) shows the logarithm spectrum values of diagonal elements from the center.

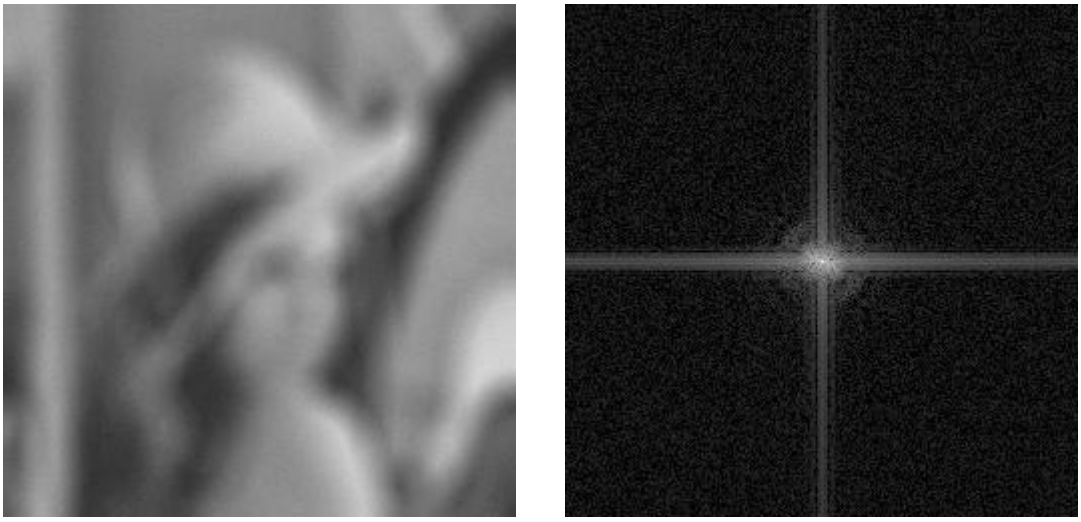

(a) (b)

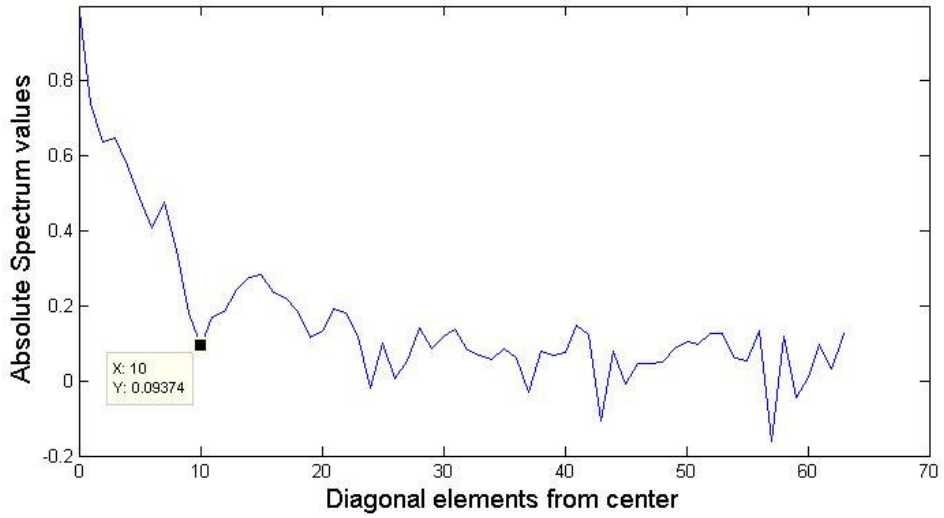

(c)

Figure 5.8 The logarithm spectrum of out of focus blurred noise added image (a) is shown in (b). (c) shows the logarithm spectrum values of diagonal elements from the center.

In the logarithm spectrum the formed circle radius values have an inverse ratio with the radius of blur kernel, $R_{\mathrm{ker}nel} \approx 1 / R_{circle}$. The disadvantageous of the logarithm spectrum is that the occurred circles can be ellipsoids due to the dimensions of the interested image. For example Peppers image size is 440×512 and logarithm spectrum is elliptical as seen in Figure 5.9. Table 5.2 shows that the observed circle radius values are not same for all images, it changes with the image dimensions. For

example the first spectral zeros for an out of focus blurring kernel of 5 pixels radius for 360×360 sized noiseless Eia image and 256×256 sized noiseless Lena image are occurred at 32^{nd} pixel and 25^{th} pixel respectively. Also the observed spectral zeros for the same sized images such as Lena and Cameraman are not same, and the logarithm spectrum method for out of focus blur identification is not robust to noise.

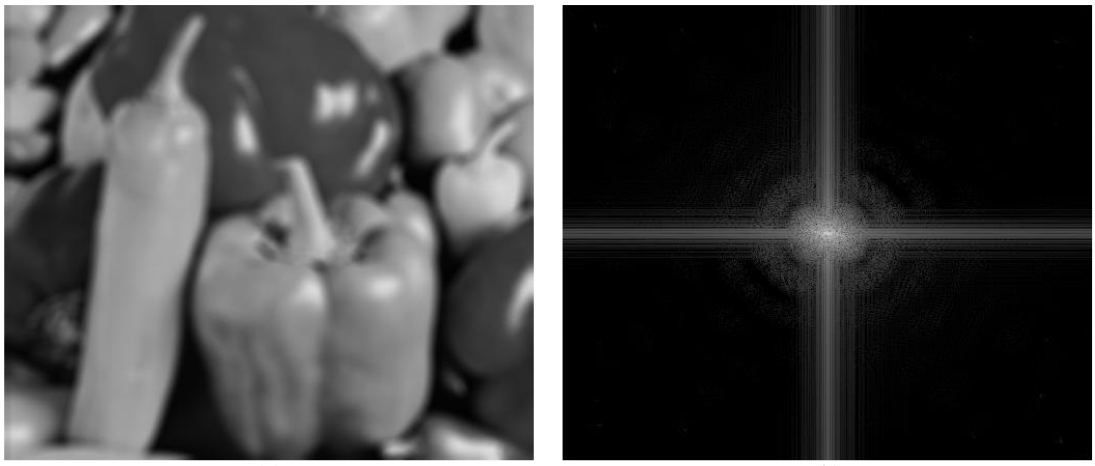

(a) (b)

Figure 5.9 The logarithm spectrum of out of focus blurred Peppers image (a) is shown in (b).

As seen from the Figures 5.10 and 5.11, which are the results of image cepstrums, the minimum values occur at the 15^{th} pixel of the diagonal for the noiseless image and at the 15^{th} pixel of the noisy out of focus blurred Cameraman images with a radius of 11 pixels. Table 5.3 shows the minimum diagonal values from the center of the other images with different radius values. To provide visibility of the normalized cepstrums, (4.13) is applied with N = 10 for noiseless frame cepstrum and N = 20 for noisy frame cepstrum. The noisy image cepstrum is smoothed with a 5×5 dimensions kernel to detect the spectral zeros easily (Figure 5.11 - d).

(a)

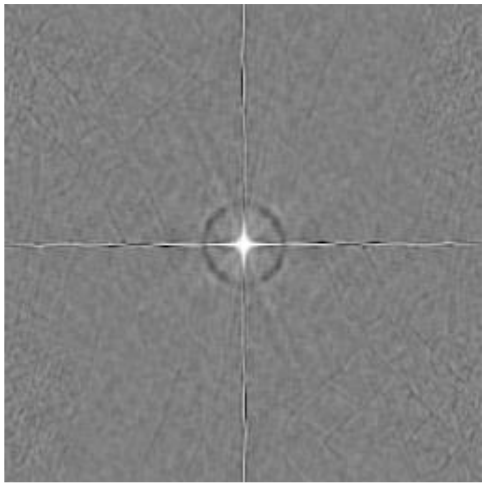

(b)

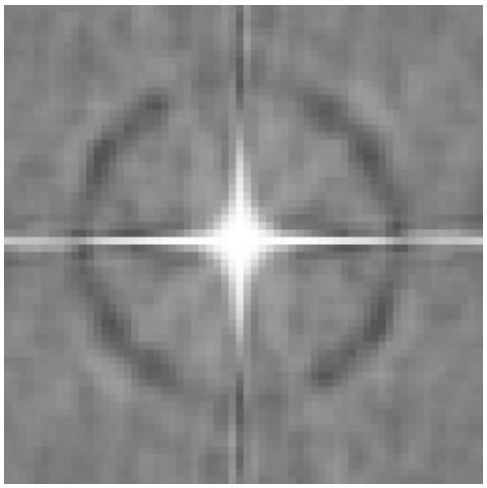

(c)

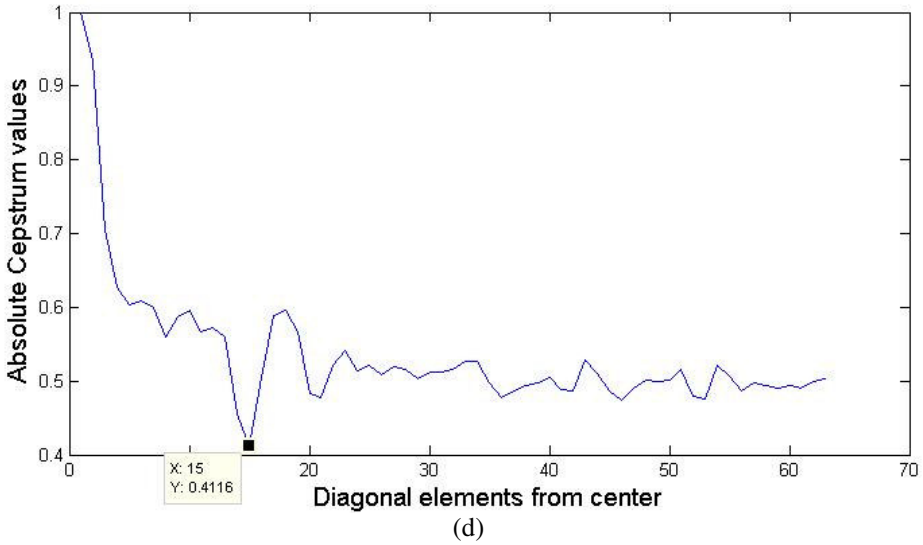

(d)

Figure 5.10 The cepstrum of blurred image (a) with an out of focus blurring kernel of radius 11 pixels is shown in (b). (c) focused center of the cepstrum. (d) shows the cepstrum values of diagonal elements from the center.

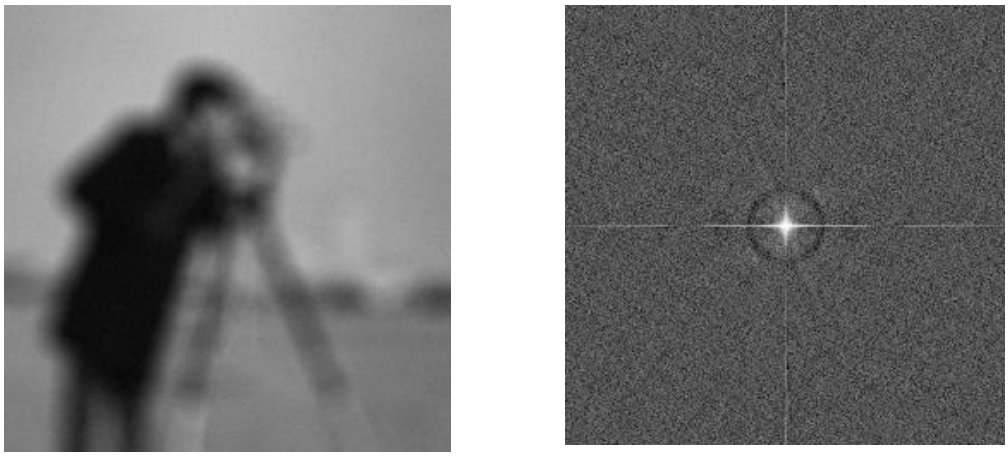

(a) (b)

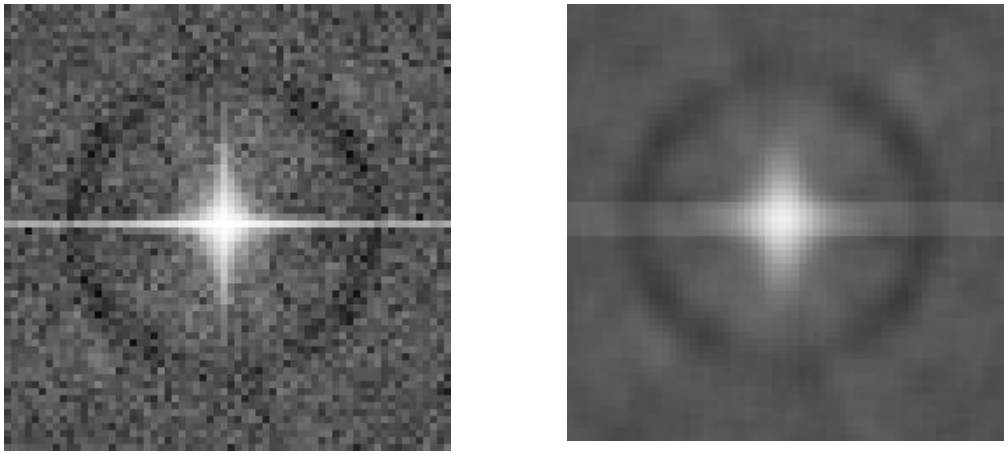

(c) (d)

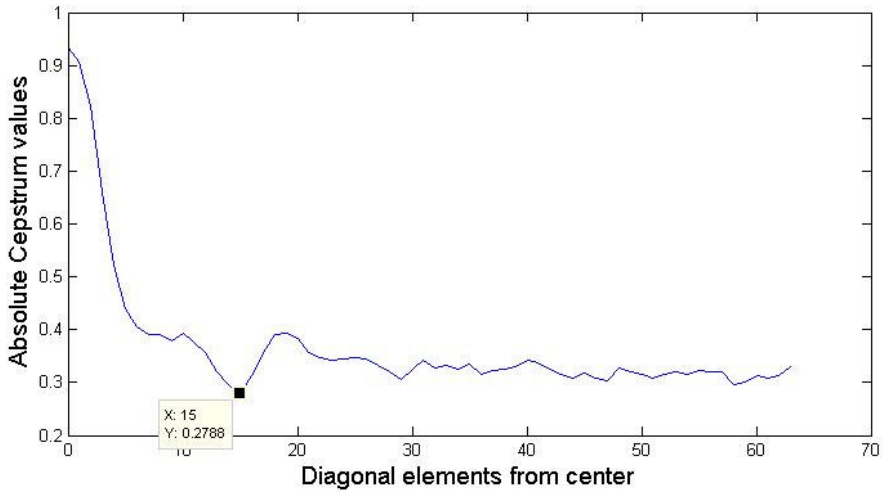

(e)

Figure 5.11 The cepstrum of blurred image (a) with an out of focus blurring kernel of radius 11 pixels and added noise is shown in (b). (c) focused center of the cepstrum. (d) shows the smoothed view of (c). (d) shows the values of diagonal elements of smoothed cepstrum values from the center.

Table 5.3 First spectral zeros of out of focus blurred images (Cepstrum method).

Image	Lena		Eia		Peppers		Cameraman	
Radius	N.less	Noisy	N.less	Noisy	N.less	Noisy	N.less	Noisy
5	7^{th} p	7^{th} p	7^{th} p	7^{th} p	7^{th} p	7^{th} p	7^{th} p	7^{th} p
7	9^{th} p	9^{th} p	9^{th} p	9^{th} p	9^{th} p	9^{th} p	9^{th} p	9^{th} p
11	15^{th} p	15^{th} p	15^{th} p	15^{th} p	15^{th} p	15^{th} p	15^{th} p	15^{th} p

As seen from the Table 5.3 cepstrum of the out of focused images is robust to noise and results do not change with the image dimensions, i.e., the observed spectral circles have the same diameters. The values are the diagonal values of the image cepstrums. The real blur kernel diameter can be calculated from these observations as follows:

$$Radius \approx \sqrt{2*\left(Observed\ Cepstrum\ Radius\right)^2}\ /\ 2 \tag{5.30}$$

As an example for radius of 11 pixels, observed cepstrum radius is 15 pixels on the diagonal and the estimated blur radius is computed as follows:

$$11 \approx \sqrt{2*15^2}\ /\ 2\ \Rightarrow 11 \approx 10{,}606$$

Also the performance is tested with real camera images beside synthetic test images. For the out of focus blur identification the bookshelf images shown in Figure 5.12 (a) and 5.13 (a) are used. The cepstrum method is applied to both of these images and the identified blurs are shown in Figure 5.12 (b) and 5.13 (b) and the blur parameters are found to be 7 pixels and 8 pixels respectively by using (5.30). It is seen that the image in Figure 5.13 (a) is more blurry and the identified blur diameter is bigger. To provide visibility of the normalized cepstrums, (4.13) is applied with N = 10 for real frame cepstrums.

(a)

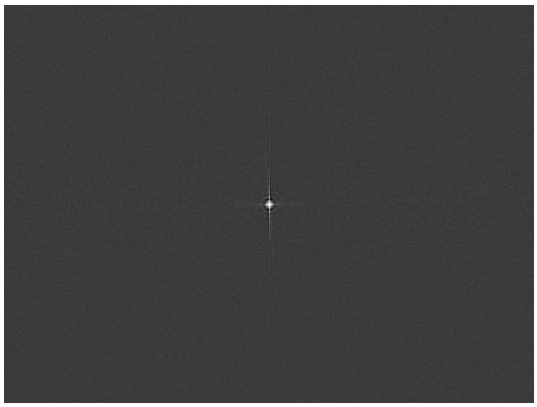

(b)

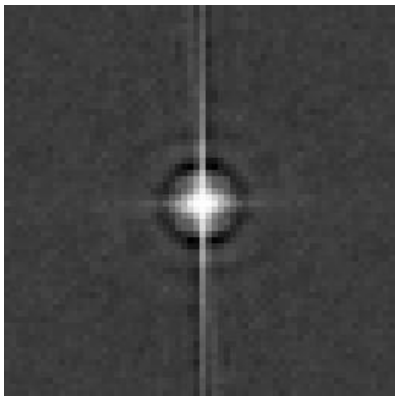

(c)

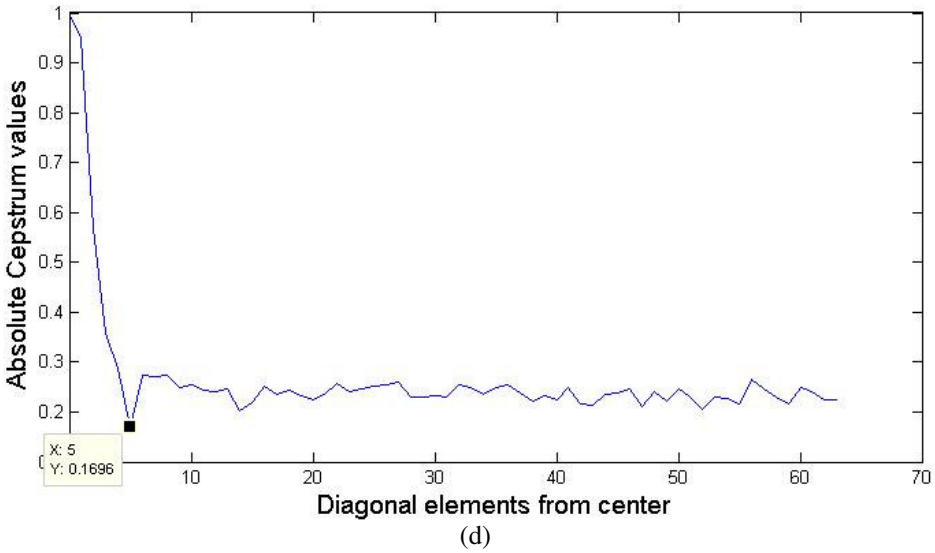

(d)

Figure 5.12 Cepstrum domain of out of focus blurred real camera image (a) is shown in (b). (c) shows the zoomed cepstrum center values. (d) shows the diagonal cepstrum elements from the center.

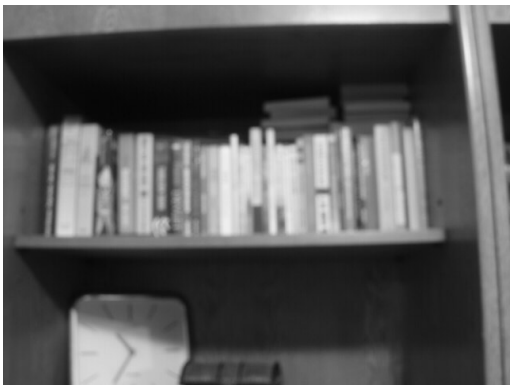

(a)

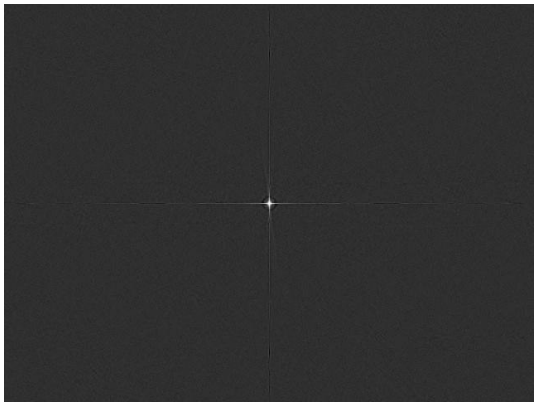

(b)

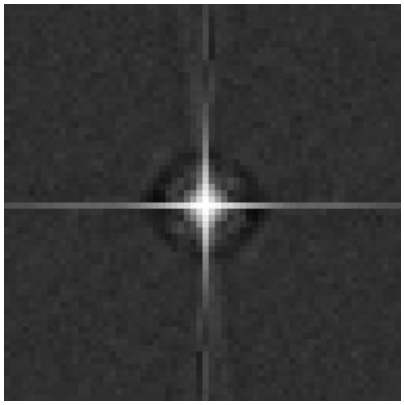

(c)

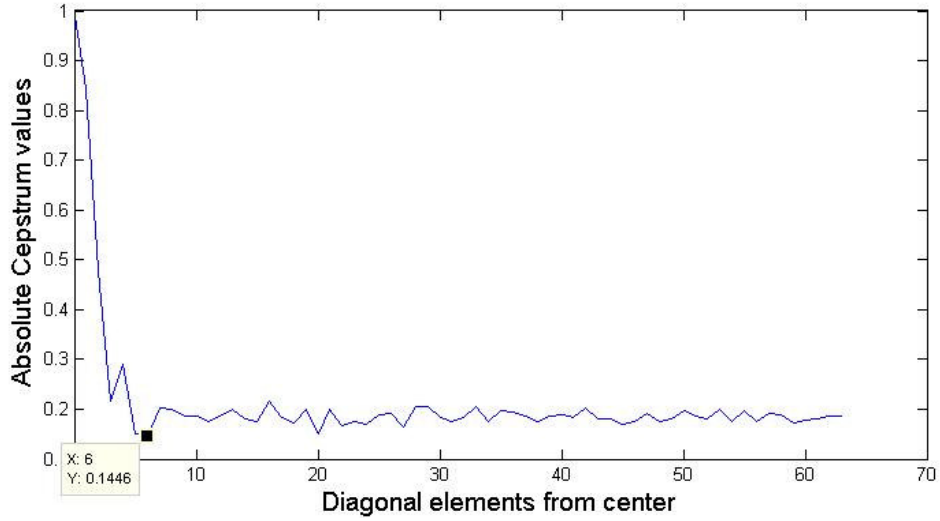

(d)

Figure 5.13 Cepstrum domain of out of focus blurred real camera image (a) is shown in (b). (c) shows the zoomed cepstrum center values. (d) shows the diagonal cepstrum elements from the center.

5.2.2. Motion Blur Identification

For the identification of motion blur, the logarithm spectrum approach [14] and the cepstrum approach [15] are tried with noiseless and noisy observations for different sized blur kernels. The methods are tried on different sized images: Lena, Eia, Peppers, and Cameraman shown in Figure 5.2. All of the images are convolved with the same blurring kernels and the results are compared.

As seen from the Figures 5.14 and 5.15, the first spectral zeros occur at the 15^{th} pixel of the diagonal from the center for the noiseless and noisy motion blurred Eia images with an angle of 45 degrees and length of 11 pixels. Table 5.4 shows the first spectral zeros of the images for different blur radius values.

Table 5.4 First spectral zeros of motion blurred images (Spectrum method).

Image	Lena		Eia		Peppers		Cameraman	
Blur Size	N.less	Noisy	N.less	Noisy	N.less	Noisy	N.less	Noisy
9x9	13^{th} p	14^{th} p	20^{th} p	20^{th} p	---	---	15^{th} p	15^{th} p
11x11	10^{th} p	10^{th} p	15^{th} p	15^{th} p	---	---	11^{th} p	11^{th} p
13x13	9^{th} p	10^{th} p	14^{th} p	14^{th} p	---	---	8^{th} p	10^{th} p

In the logarithm spectrum, the first spectral zero values have an inverse ratio with the size of blur kernel, $S_{\ker nel} \alpha (1 / S_{zeros})$. The disadvantageous of the logarithm spectrum is that the occurred spectral zero angles can be changed due to the dimensions of the interested image. For example (440×512) pixels sized Peppers image seen in Figure 5.16. Table 5.4 shows that the spectral zeros do not occur on the same points for the same sized images such as Lena and Cameraman. Also the logarithm spectrum method is not robust to noise for motion blur identification.

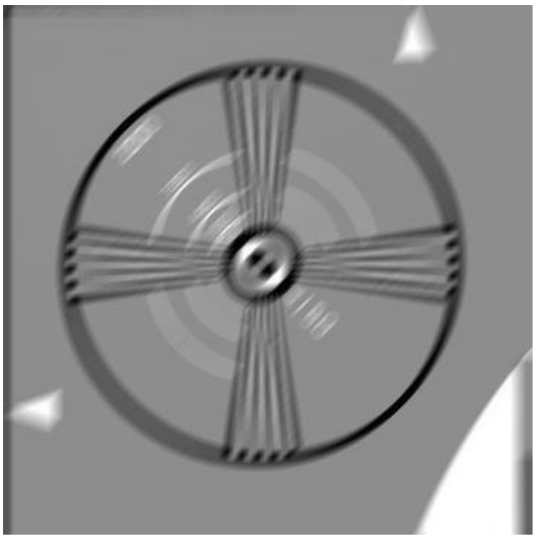

(a)

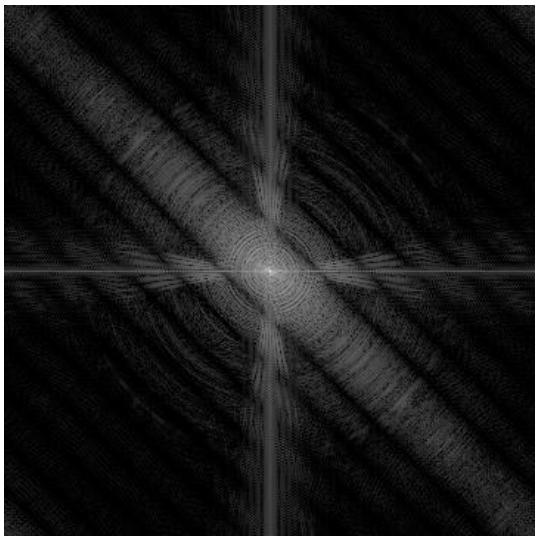

(b)

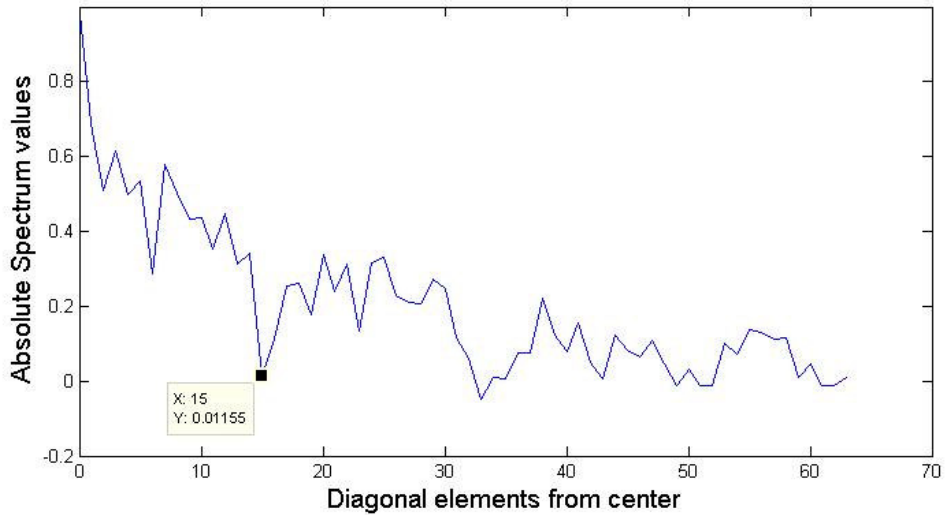

(c)

Figure 5.14 Logarithm spectrum of motion blurred noiseless Eia image (a) 11 pixels length motion blur kernel with an angle of 45 is shown in (b). (c) shows the logarithm spectrum values of diagonal elements from the center.

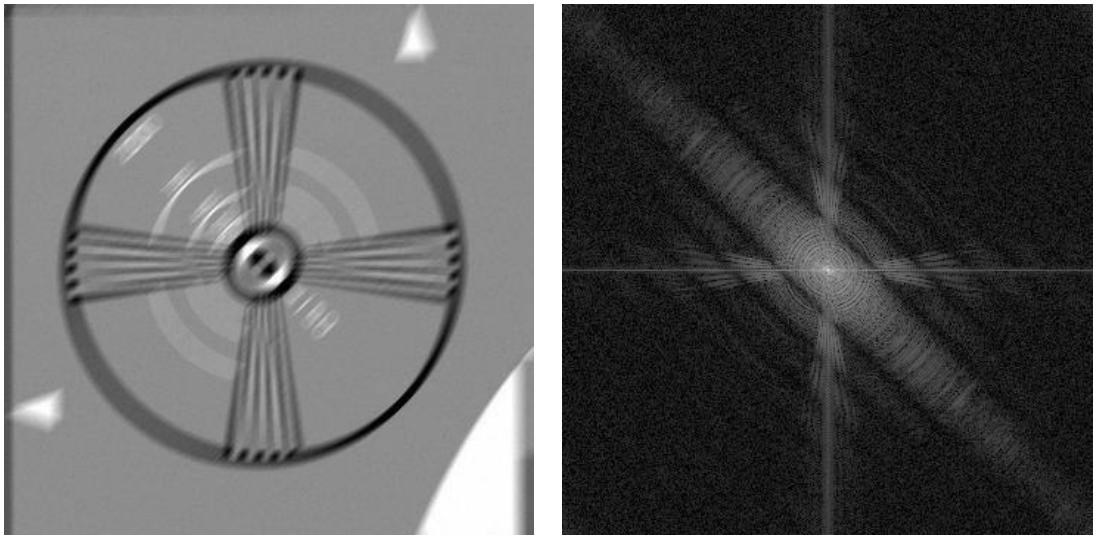

(a) (b)

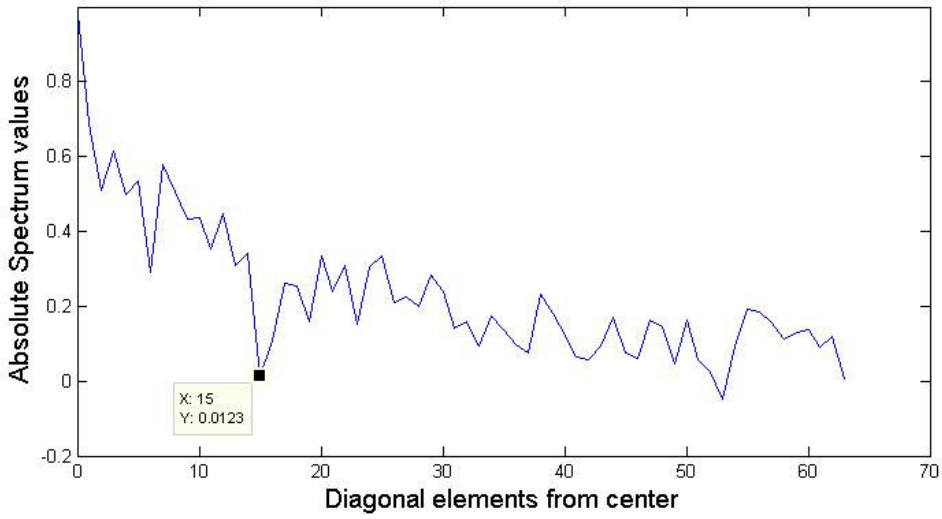

(c)

Figure 5.15 Logarithm spectrum of motion blurred noisy Eia image (a) 11 pixels length motion blur kernel with an angle of 45 is shown in (b). (c) shows the logarithm spectrum values of diagonal elements from the center.

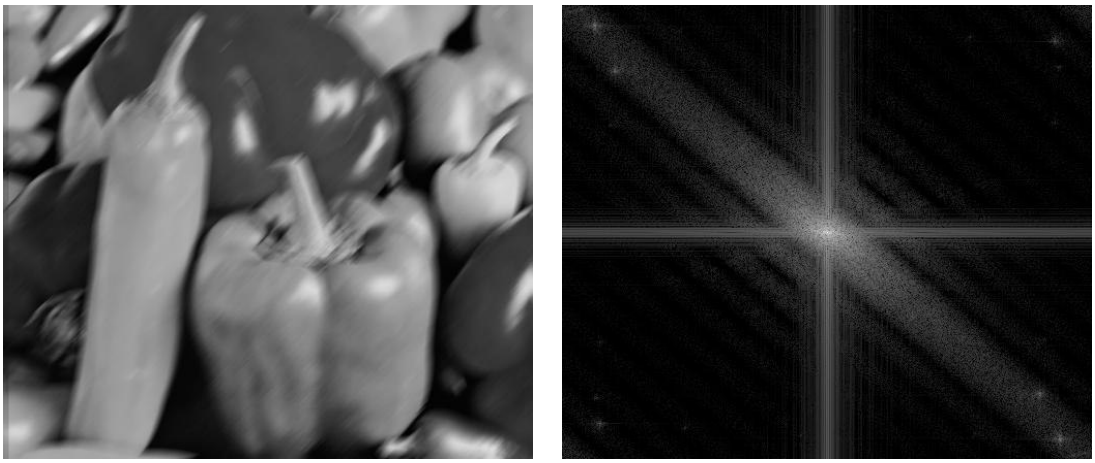

(a) (b)

Figure 5.16 Logarithm spectrum of motion blurred noiseless Peppers image (a) by 11 pixels length motion blur kernel with an angle of 45 is shown in (b).

As seen from the Figures 5.17 and 5.18, which are the results of image cepstrums, the minimum values occur at the 11^{th} pixel of the diagonal for the noiseless image and at the 11^{th} pixel of the noisy out of focus blurred Cameraman images with an angle of 45 degrees and length of 11 pixels. Table 5.5 shows the minimum diagonal values from the center of the other images with different radius values. To provide visibility of the normalized cepstrums, (4.13) is applied with N = 10 for noiseless and noisy frame cepstrums.

Table 5.5 First spectral zeros of motion blurred images (Cepstrum method).

Image Radius	Lena		Eia		Peppers		Cameraman	
	N.less	Noisy	N.less	Noisy	N.less	Noisy	N.less	Noisy
5	5^{th} p	5^{th} p	5^{th} p	5^{th} p	5^{th} p	5^{th} p	5^{th} p	5^{th} p
7	7^{th} p	7^{th} p	7^{th} p	7^{th} p	7^{th} p	7^{th} p	7^{th} p	7^{th} p
11	11^{th} p	11^{th} p	11^{th} p	11^{th} p	11^{th} p	11^{th} p	11^{th} p	11^{th} p

As seen from the Table 5.5 cepstrum of the motion blurred images is robust to noise and the results do not change with the image dimensions, the observed spectral zeros occurred in the same locations.

(a)

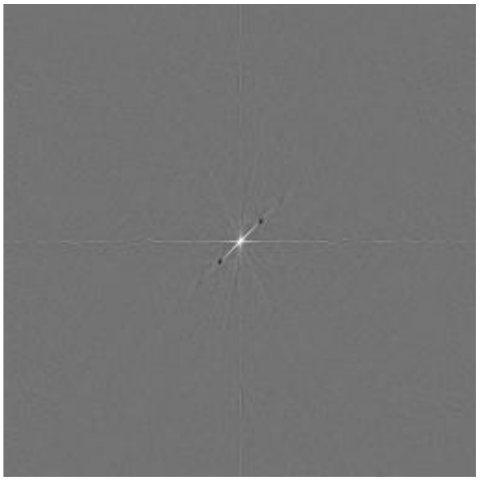

(b)

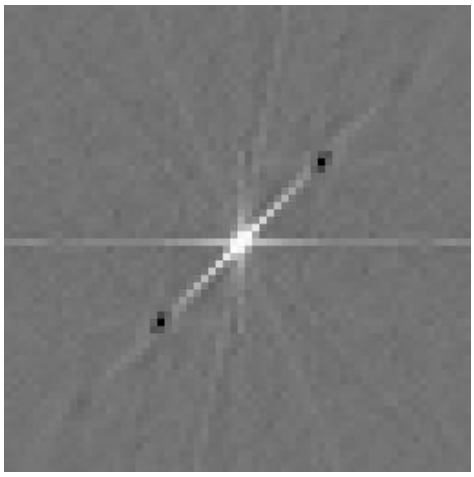

(c)

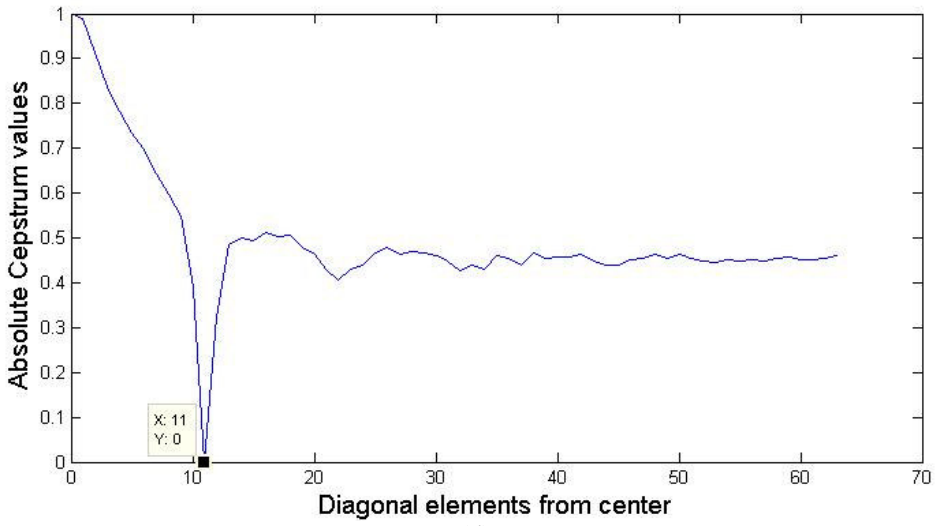

(d)

Figure 5.17 Cepstrum of noiseless motion blurred Cameraman image (a) by 11 pixels length motion blur kernel with an angle of 45 is shown in (b). (c) shows the cepstrum values of diagonal elements from the center.

(a)

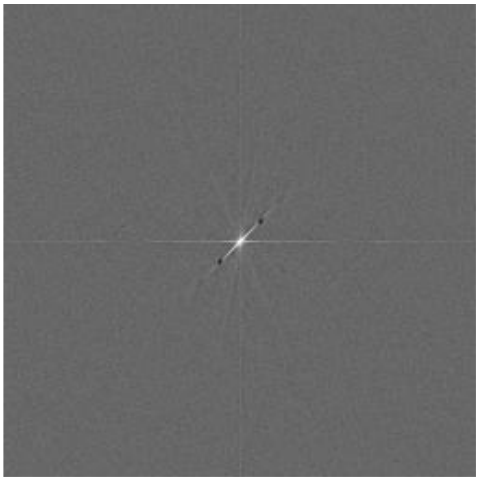

(b)

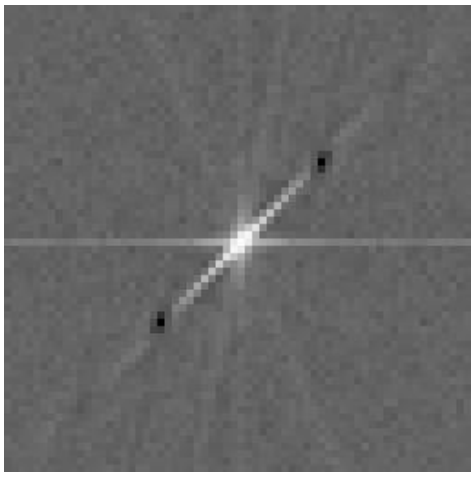

(c)

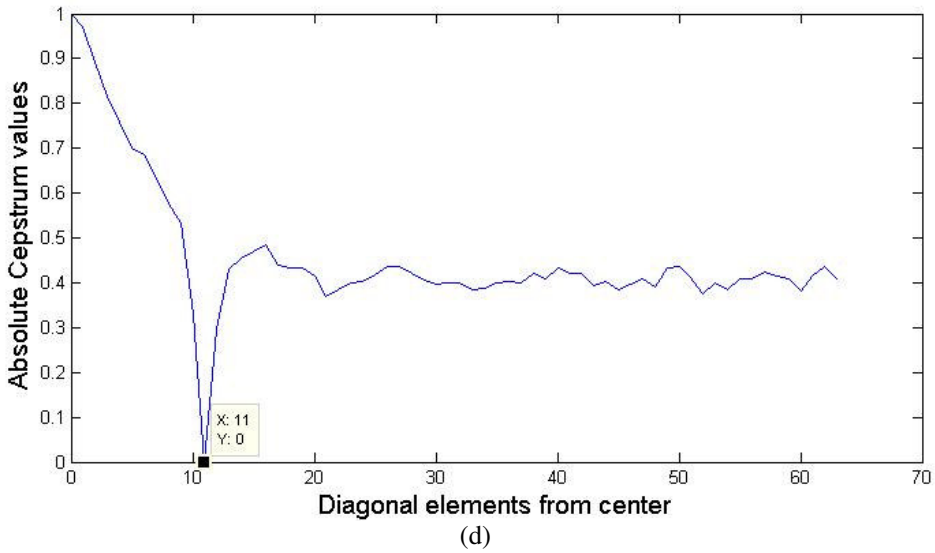

(d)

Figure 5.18 Cepstrum of noisy motion blurred Cameraman image (a) by 11 pixels length motion blur kernel with an angle of 45 is shown in (b). (c) shows the cepstrum values of diagonal elements from the center.

5.2.3. Gaussian Blur Identification

For the identification of Gaussian blur, the Kurtosis minimization method [19] and the ARMA approach [16-18] are tried with noiseless and noisy observations for different sized blur kernels. The methods are tried on different sized images: Lena, Eia, Peppers, and Cameraman shown in Figure 5.2. All of the images are convolved with the same blurring kernels and the results are compared.

Kurtosis minimization method is tried with the test images for Gaussian blur identification. The images are first blurred with different known blur variances. Then the blurred images are deconvolved with wiener filter for different sized blur kernels with different variances. And the original blur kernels and the kernels that result the minimum Kurtosis value are shown in Table 5.6.

Table 5.6 Real and identified Gaussian blur kernels with Kurtosis Minimization.

Image	Original Blur Kernel Size & Variance	Blur Kernel Size and Blur Variance with minimum Kurtosis value
Lena	7 x 7 pixels & σ (blur) = 1.5	5 x 5 pixels & σ (blur) = 1.2
Peppers	7 x 7 pixels & σ (blur) = 1.1	5 x 5 pixels & σ (blur) = 0.1
Eia	9 x 9 pixels & σ (blur) = 1.9	9 x 9 pixels & σ (blur) = 1.9
Cameraman	7 x 7 pixels & σ (blur) = 2.0	7 x 7 pixels & σ (blur) = 2.0

It is clearly seen from Table 5.6 that Kurtosis minimization approach for Gaussian blur kernel identification is not successful for all images.

Figures 5.19 and 5.20 show the results of Gaussian blur identification method ARMA. It can be clearly seen that the deconvolved images of blurred one with the original blur kernel and with the estimated blur kernel are closer.

(a) (b)

(c) (d)

Figure 5.19 The Lena image (a) is blurred by a kernel of 7×7 pixels with variance 1.5. (c) and (d) shows the deblurred images with estimated parameters and original parameters respectively.

(a) (b)

(c) (d)

Figure 5.20 The Cameraman image (a) is blurred by a kernel of 7×7 pixels with variance 2.5. (c) and (d) shows the deblurred images with estimated parameters and original parameters respectively.

5.3. Superresolution with Identified Blur Parameters

In this part, the proposed SR reconstruction method, MAP based BTV approach, is handled with identified blur parameters by the methods described in Section 5.2.

The regularization parameter λ is chosen as 0.3, α is chosen as 0.4, β is chosen as 0.002 and P = 2 for BTV regularization term. The initial estimate of the image $\hat{x}$ is chosen as the pixel medians of bilinear interpolated LR image frames.

5.3.1. Out of Focus Blur Estimation and Superresolution

For the implementation, the used test images are shifted with known subpixel values and convolved with blur kernels with diameters 3, 5 and 7 pixels for different test conditions. The blurred images are then downsampled. Images are registered after the Gaussian noise is added. For each test image five LR images are created. The initial estimate HR frames are created by the pixel medians of the bilinear interpolated versions of the registered LR frames. Table 5.7 shows the real blur kernels and the identified blur kernels from initial estimates of the HR grid image by using the cepstrum method.

Table 5.7 Real and estimated Out of Focus Blur parameters.

Image	Real Blur Kernels		
	3 pixels	5 pixels	7 pixels
Cameraman	2,8284 ≈ 3	5,6568 ≈ 5	7,0710 ≈ 7
Eia	2,8284 ≈ 3	5,6568 ≈ 5	7,0710 ≈ 7
Lena	2,8284 ≈ 3	5,6568 ≈ 5	7,0710 ≈ 7
Peppers	2,8284 ≈ 3	5,6568 ≈ 5	7,0710 ≈ 7

Table 5.8 shows the BTV approach results of the test images, PSNR and MSE are used for scalar comparison. Also Figures 5.21 – 5.23 show the visual improvement of the LR images.

Table 5.8 Iteration results of Out of Focus blurred Images.

Blur Kernel Diameter	Cameraman		Eia		Lena		Peppers	
	MSE	PSNR	MSE	PSNR	MSE	PSNR	MSE	PSNR
3	0,0090	25,9560	0,0100	24,6912	0,0038	29,4707	0,0029	31,6559
Initial Image	0,0145	23,8909	0,0245	20,8134	0,0075	26,4900	0,0049	28,8139
5	0,0098	25,6007	0,0097	24,8605	0,0044	28,7669	0,0026	31,6077
Initial Image	0,0169	23,2247	24,8605	19,7491	0,0091	25,6311	0,0058	28,0789
7	0,0125	24,2114	0,0194	21,8342	0,0059	27,5579	0,0032	30,5792
Initial Image	0,0214	22,2161	0,0447	18,2074	0,0120	24,4410	0,0076	26,9073

(a) (b)

(c) (d)

Figure 5.21 The Cameraman image (a) is blurred by an out of focus blurring kernel of 3 pixels diameter and down sampled by a factor of two in both dimensions and added noise (b). (c) is the pixel medians of bilinear interpolated registered LR frames. (d) is the superresolved image.

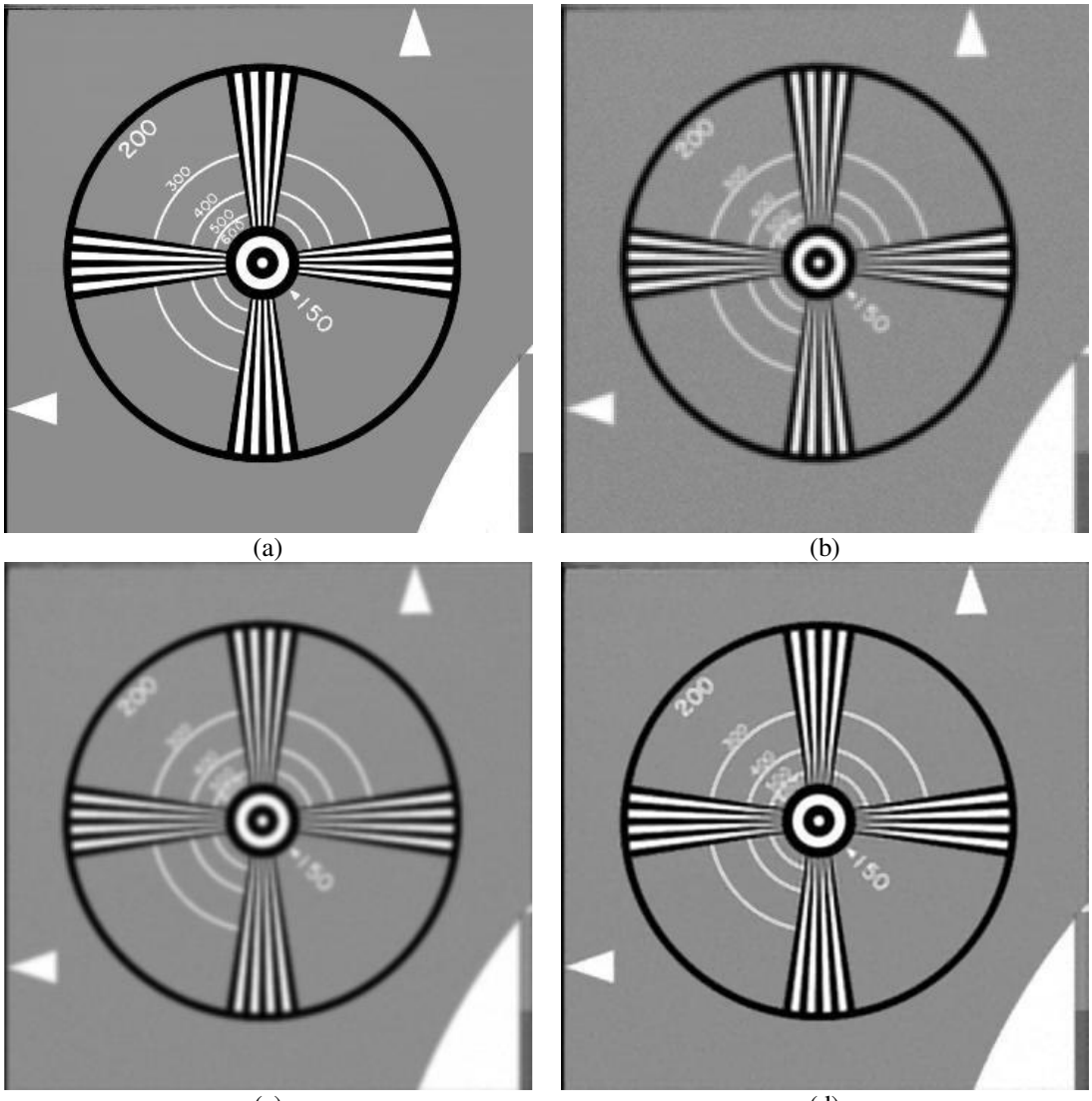

Figure 5.22 The Eia image (a) is blurred by an out of focus blurring kernel of 5 pixels diameter and down sampled by a factor of two in both dimensions and added noise (b). (c) is the pixel medians of bilinear interpolated registered LR frames. (d) is the superresolved image.

(a) (b)

(c) (d)

Figure 5.23 The Lena image (a) is blurred by an out of focus blurring kernel of 7 pixels diameter and down sampled by a factor of two in both dimensions and added noise (b). (c) is the pixel medians of bilinear interpolated registered LR frames. (d) is the superresolved image.

5.3.2. Motion Blur Estimation and Superresolution

This type of SR can be possible for the video frames with a motion with constant speed and angle. The interested parts of video frames, where the dimensions are smaller than the video frame, must be registered then the proposed methods must be applied. For instance, when a 40×40 sizes part of a video frame of sizes 640×480 with a motion of 7 pixels speed and 45 degree angles is handled, the interested part will be approximately shifted 7 pixels with 45 degrees in each frame of the video one after another. When these interested parts of the motion blurred frames are registered, it will be possible to use SR techniques.

For the implementation, the used test images are shifted with known subpixel values and convolved by blur kernels with 45 degree angles and 5, 7 and 9 pixel motions for different test conditions. The blurred images are then downsampled. Images are registered after the Gaussian noise is added. For each test image five LR images are created. The initial estimate HR frames are created by the pixel medians of the bilinear interpolated versions of the registered LR frames. Table 5.9 shows the real blur kernels and the identified blur kernels from initial estimates of the HR grid image by using the cepstrum method.

Table 5.9 Real and estimated Motion Blur parameters.

Image	45 degrees & 5 pixels	45 degrees & 7 pixels	45 degrees & 9 pixels
Cameraman	5 pixels	7 pixels	9 pixels
Eia	5 pixels	7 pixels	9 pixels
Lena	5 pixels	7 pixels	9 pixels
Peppers	5 pixels	7 pixels	9 pixels

Table 5.10 shows the BTV approach results of the test images, PSNR and MSE are used for scalar comparison. Also Figures 5.24 – 5.26 show the visual improvement of the LR images.

Table 5.10 Iteration results of Motion blurred Images.

Angle & Motion	Cameraman		Eia		Lena		Peppers	
	MSE	PSNR	MSE	PSNR	MSE	PSNR	MSE	PSNR
45 degrees & 5 pixels	0,0173	24,0076	0,0175	22,2655	0,0049	28,2281	0,0028	31,2387
Initial Image	0,0200	22,5005	0,0425	18,4203	0,0105	25,0383	0,0071	27,1902
45 degrees & 7 pixels	0,0128	24,4440	0,0309	19,8129	0,0056	27,7521	0,0044	29,2380
Initial Image	0,0252	21,5041	0,0619	16,7915	0,0138	23,8377	0,0096	25,8773
45 degrees & 9 pixels	0,0139	24,0812	0,0476	17,9287	0,0064	27,1643	0,0049	28,7909
Initial Image	0,0299	20,7585	0,0793	15,7163	0,0171	22,9016	0,0122	24,8225

(a) (b) (c) (d)

Figure 5.24 The Cameraman image (a) is blurred by a motion blurring kernel of 5 pixels length with an angle of 45 degrees and down sampled by a factor of two in both dimensions and added noise (b). (c) is the pixel medians of bilinear interpolated registered LR frames. (d) is the superresolved image.

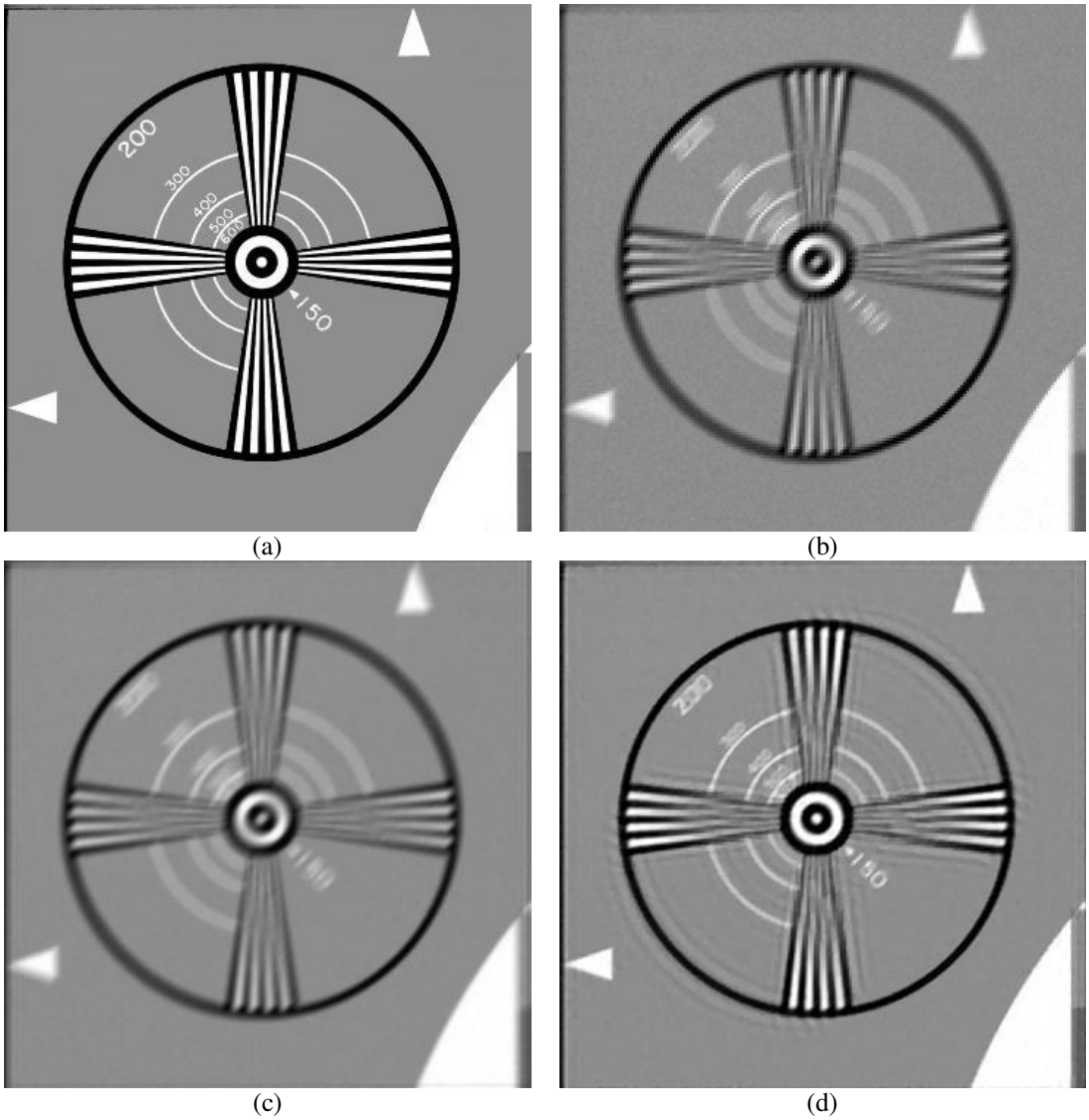

(a) (b)

(c) (d)

Figure 5.25 The Eia image (a) is blurred by a motion blurring kernel of 7 pixels length with an angle of 45 degrees and down sampled by a factor of two in both dimensions and added noise (b). (c) is the pixel medians of bilinear interpolated registered LR frames. (d) is the superresolved image.

(a) (b)

(c) (d)

Figure 5.26 The Lena image (a) is blurred by a motion blurring kernel of 9 pixels length with an angle of 45 degrees and down sampled by a factor of two in both dimensions and added noise (b). (c) is the pixel medians of bilinear interpolated registered LR frames. (d) is the superresolved image.

5.3.3. Gaussian Blur Estimation and Superresolution

For the implementation, the used test images are shifted with known subpixel values and convolved by (7×7) sized blur kernels with variances 1.1 and 2.5 for different test conditions. The blurred images are then downsampled. Images are registered after the Gaussian noise is added. For each test image five LR images are created. The initial estimate HR frames are created by the pixel medians of the bilinear interpolated versions of the registered LR frames. Table 5.11 shows the results of BTV algorithm applied with the original blur kernel values and identified blur kernel values from initial estimates of the HR grid image by using the ARMA method. PSNR and MSE are used for scalar comparison. Also Figures 5.27 – 5.29 show the visual improvement of the LR images.

Table 5.11 Iteration results of Gaussian blurred Images.

IMAGE	Blur Parameters	Blur Variance σ = 1.1		Blur Variance σ = 2.5	
		MSE	PSNR	MSE	PSNR
Cameraman	Identified Blur	0,0116	24,8587	0,0177	23,0413
	Original Blur	0,0097	25,6613	0,0136	24,1667
Initial Cameraman Image		0,0171	23,1915	0,0232	21,8671
Eia	Identified Blur	0,0119	23,9349	0,0338	19,4189
	Original Blur	0,0096	24,8697	0,0248	20,7556
Initial Eia Image		0,0320	19,6622	0,0516	17,5816
Lena	Identified Blur	0,0055	27,8499	0,0092	25,6113
	Original Blur	0,0043	28,8834	0,0066	27,0399
Initial Lena Image		0,0091	25,6238	0,0133	23,9975
Peppers	Identified Blur	0,0039	29,7286	0,0053	28,4098
	Original Blur	0,0025	31,6788	0,0041	29,5666
Initial Peppers Image		0,0058	28,0407	0,0084	26,4306

(a)

(b)

(c)

(d)

(e)

Figure 5.27 The Cameraman image (a) is blurred by a Gaussian blurring kernel of (7×7) pixels with a variance of 1.1 and down sampled by a factor of two in both dimensions and added noise (b). (c) is the pixel medians of bilinear interpolated registered LR frames. (d) and (e) are the superresolved images of estimated parameters and original parameters respectively.

(a)

(b)

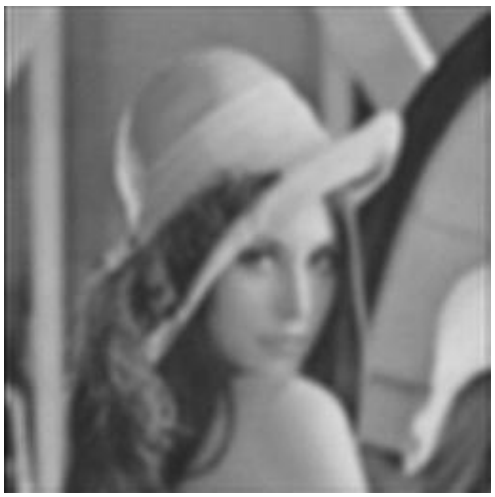

(c)

(d)

(e)

Figure 5.28 The Lena image (a) is blurred by a Gaussian blurring kernel of (7×7) pixels with a variance of 2.5 and down sampled by a factor of two in both dimensions and added noise (b). (c) is the pixel medians of bilinear interpolated registered LR frames. (d) and (e) are the superresolved images of estimated parameters and original parameters respectively.

(a)

(b)

(c)

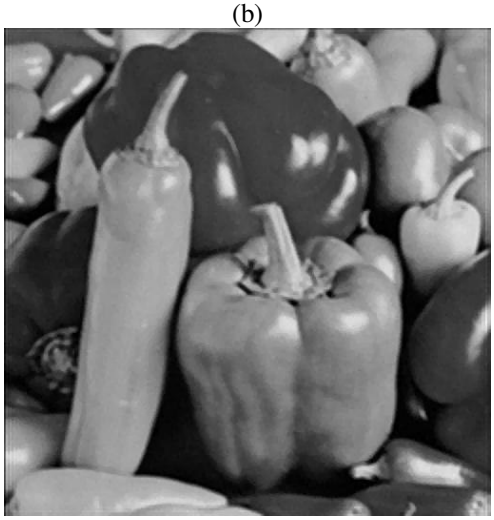

(d)

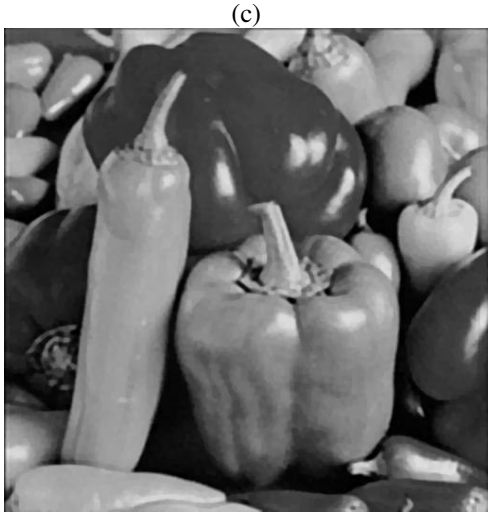

(e)

Figure 5.29 The Peppers image (a) is blurred by a Gaussian blurring kernel of (7×7) pixels with a variance of 2.5 and down sampled by a factor of two in both dimensions and added noise (b). (c) is the pixel medians of bilinear interpolated registered LR frames. (d) and (e) are the superresolved images of estimated parameters and original parameters respectively.

CHAPTER 6

CONCLUSIONS

In this thesis, the Maximum a Posteriori method, one of the stochastic approaches, is examined with different regularization terms and fidelity terms for SR image reconstruction from multiple registered images. The main idea of SR image reconstruction is to reach an upper sized and more detailed image by combining the knowledge of the LR images to a HR image grid. But during the record period of the scene some unwanted conditions like blur, decimation, noise, warping, degrade the image information, and cause the SR image reconstruction become an ill posed inverse problem.

As SR image reconstruction is an ill posed inverse problem, the operators that degrade the image must be all known or must be estimated / identified close to the actual values to reach the best superresolved images.

In our implementations we accepted that the warping operators were all known and we focused on the blurring operators. The blur models and the identification methods are tried and their performances are shown. The critical point which should be emphasized is that the blur identification methods are all used in SR image restoration algorithms in the literature. But we have showed that these methods can also be used in SR reconstruction algorithms. For the out of focus blur and motion blur identification the logarithm spectrum and the cepstrum methods are tried. Logarithm spectrum method is not useful for general case, because the identified values and shapes change due to the image dimensions and the image itself. But the cepstrum blur identification method satisfies the same results for all images even though the images are same sized or not. For the Gaussian blur estimation Kurtosis

minimization based method and ARMA model are used and the results are shown. Kurtosis minimization method is not useful for general case, because the estimated / identified values are not true for all images. On the other hand, ARMA is an optimization based estimation technique. The reached values are not the real values but they converge to the real values, if initial values could be determined well.

MAP Estimation maximizes the likelihood of HR image given LR images with the priori knowledge (regularization term). Different types of regularization terms and data fidelity terms are tried and performance tests are compared. L1 Norm Fidelity term with BTV and TV type regularization terms have given the best results.

The experiments show that noise is very effective on the blur identification methods and the performance of SR algorithms. If the amount of noise is higher, identification of blur parameters is getting hard, and blur identification becomes impossible after a certain amount of noise. But there are no distinct threshold values that can be considered to frustrate blur identification.

Consequently, if we consider about the general SR algorithms, the degradation parameters have to be estimated before they are applied to reach the best superresolved image. The biggest challenge of the parameter estimation / identification methods is caused by the system noise. Our studies will continue on the removal of noise effect before any parameter estimation and on the estimation of warping parameters, which are assumed to be known in this thesis study.

REFERENCES

[1] R. Y. Tsai and T. S. Huang, "Multiframe image restoration and registration" in Advances in Computer Vision and Image Processing, T. S. Huang, Ed. JAI Press, vol. 1, 1984, pp. 317 – 339.

[2] S. P. Kim, N. K. Bose, and H. M. Valenzuela, "Recursive reconstruction of high resolution image from noisy undersampled multiframes", IEEE Trans. on Acoustics, Speech and Signal Processing, vol. 38, no. 6, 1990, pp. 1013 – 1027.

[3] A. M. Tekalp, M. K. Özkan, and M. I. Sezan, "High-resolution image reconstruction from lower-resolution image sequences and space varying image restoration", in Proc. IEEE Int. Conf. Acoustics, Speech and Signal Processing (ICASSP), San Francisco, CA., vol. 3, Mar. 1992, pp. 169 – 172.

[4] J. L. Brown, "Multichannel sampling of low-pass signals", IEEE Transactions on Circuits and Systems, vol. 28, no. 2, 1981, pp. 101 – 106.

[5] A. Papoulis, "Generalized sampling expansion", IEEE Transactions on Circuits and Systems, vol. 24, no. 11, Nov. 1977, pp. 652 – 654.

[6] S. Borman and R. L. Stevenson, "Super-resolution from image sequences - A review", in Proc. 1998 Midwest Symp. Circuits and Systems, 1999, pp. 374 – 378.

[7] M. Irani and S. Peleg, "Super Resolution from Image Sequences", in Proc. of the 10th International Conference on Pattern Recognition, Atlantic City, NJ, vol. 2, June 1990, pp. 115 – 120.

[8] M. Irani and S. Peleg, "Motion analysis for image enhancement: Resolution, occlusion and transparency", Journal of Visual Communications and Image Representation, vol. 4, Dec. 1993, pp. 324–335.

[9] H. Wei and T. D. Binnie, "High-Resolution Image Reconstruction from Multiple Low-Resolution Images", in Image Processing and Its Applications, Conference Publication No. 465 IEE, 1999.

[10] D. Youla and H. Webb, "Image restoration by the method of convex projections: Part 1 – Theory", IEEE Transactions on Medical Imaging, October 1982, pp. 81 – 94.

[11] M. Elad and A. Feuer, "Restoration of a Single Superresolution Image from Several Blurred, Noisy, and Undersampled Measured Images", IEEE Trans. On Image Processing, Vol. 6, No. 12, December 1997, pp. 1646 – 1658.

[12] T. Wang, Y. Zhang, Y. S. Zhang and L. X. Lin, "Automatic Super-resolution Image Reconstruction Based on Hybrid MAP – POCS", IEEE Proceedings of the 2007 International Conference on Wavelet Analysis and Pattern Rec., Beijing, China, 2 – 4 November 2007, pp. 426 – 431.

[13] R. L. Lagendijk and J. Biemond, "Basic Methods for Image Restoration and Identification", on Elsevier Academic Press 2005, pp. 167 – 181.

[14] M. E. Moghaddam, "A Mathematical Model to estimate Out of Focus Blur", IEEE Proceedings of the 5th International Symposium on Image and Signal Processing and Analysis 2007, pp. 278 – 281.

[15] S. Wu, Z. Lu, E. P. Ong and W. Lin, "Blind Image Blur Identification in Cepstrum Domain", IEEE Proceedings of 16th International Conference on Computer Communications and Networks, 2007, pp. 1166 – 1171.

[16] A. M. Tekalp, H. Kaufman and J. W. Woods, "Identification of Image and Blur Parameters for the Restoration of Non-causal Blurs", IEEE Transactions On Acoustics, Speech and Signal Processing, 34, 1986, pp. 963 – 972.

[17] A. Kızılkaya and H. Kayran, "EAR model yaklaşımını kullanarak 2-B ARMA model parametrelerinin kestirimi", İTÜ Mühendislik Dergisi, Vol. 5, No.4, August 2006, pp. 10 – 22.

[18] N. Y. Sarı and A. H. Kayran, "Simultaneous Identification of Image and Blur Parameters with the 2-D Hybrid Lattice Structure", IEEE Proceedings, 13th Signal Processing and Communications Applications Conference, May 2005, pp. 312 – 315.

[19] D. Li, R. M. Mersereau and S. Simske, "Blur Identification Based on Kurtosis Minimization", IEEE International Conference on Image Processing, 2005, pp. 905 – 908.

[20] H. Hu and G. D. Haan, "Low Cost Blur Estimator", IEEE International Conference on Image Processing, October 2006, pp. 617 – 620.

[21] F. Rooms, M. Ronsse, A. Pizurica, and W. Philips, "PSF estimation with applications in autofocus and image restoration", in 3rd IEEE Benelux Signal Processing Symposium, 2002, pp. 13 – 16.

[22] S. Farsiu, M. D. Robinson, M. Elad and P. Milanfar, "Fast and Robust Multiframe Super Resolution", IEEE Transactions on Image Processing, Vol. 13, No. 10, October 2004, pp. 1327 – 1344.

[23] D. Rajan and S. Chaudhuri, "Generation Of Super-Resolution Images From Blurred Observations Using Markov Random Fields", IEEE International Conference on Acoustics, Speech, and Signal Processing Proceedings, 2001, pp. 1837 – 1840.

[24] D. Rajan and S. Chaudhuri, "An MRF-Based Approach to Generation of Super-Resolution Images from Blurred Observations", Journal of Mathematical Imaging and Vision, Vol. 16, 2002, pp. 5 – 15.

[25] N. K. Bose, M. K. Ng and A. C. Yau, "Super-Resolution Image Restoration from Blurred Observations", IEEE International Symposium on Circuits and Systems, 2005, pp. 6296 – 6299.

[26] S. Farsiu, D. Robinson, M. Elad and P. Milanfar, "Advances and Challanges in Super – Resolution", International Journal of Imaging Systems and Technology, Volume 14, No 2, August 2004, pp. 47 – 57.

[27] S. C. Park, M. K. Park and M. G. Kang, "Superresolution Image Reconstruction: A Technical Overview", IEEE Signal Processing Magazine, Vol. 20, Issue 3, May 2003, pp. 21 – 36.

[28] K. Özkan, "Reconstruction of a Single High Resolution Image from Low Resolution Images", Doctoral Dissertation, Eskişehir Osmangazi University Graduate School of Natural and Applied Sciences, March 2007.

[29] A. J. Patti, M. İ. Sezant, and A. M. Tekalp "High – Resolution Image Reconstruction from a Low – Resolution Image Sequence In The Presence of Time – Varying Motion Blur", IEEE Image Processing Proceedings, 1994, Vol. 1, Nov. 1994, pp. 343 – 347.

[30] O. A. Omer and T. Tanaka, "Joint Blur Identification and High – Resolution Image Estimation Based on Weighted Mixed – Norm with Outlier Rejection", IEEE International Conference on Acoustics, Speech and Signal Processing, 2008, pp. 1305 – 1308.

[31] Wikipedia, The Free Encyclopedia, http://en.wikipedia.org/wiki/Maximum_a_posteriori, last accessed date: 03/06/2008